

https://dspace.org/

Development of new radiation hard materials with high secondary electron emission yield for the nuclear industry

Baldwin, Cameron Lance

2025-09
University of the Witwatersrand, Johannesburg
https://hdl.handle.net/10539/50141
Baldwin, Cameron Lance. (2025). Development of new radiation hard materials with high secondary electron emission yield for the nuclear industry. [Master's dissertation, University of the Witwatersrand, Johannesburg]. WIReDSpace. https://hdl.handle.net/10539/50141

Downloaded from a DSpace repository. https://dspace.org/

Development of new radiation hard materials with high secondary electron emission yield for the nuclear industry

Cameron Lance Baldwin



UNIVERSITY OF THE
WITWATERSRAND,
JOHANNESBURG

A report submitted as the requirements for an MSc by dissertation

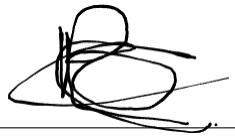
The University of the Witwatersrand
School of Physics
Johannesburg, South Africa

September 2025

Supervisor Professor Elias Sideras-Haddad

Declaration

I declare that this dissertation is my own, unaided work. It is being submitted for the degree of master of science in physics at the University of the Witwatersrand, Johannesburg. It has not been submitted before for any degree or examination at any other University.



2025/09/09

Cameron Baldwin

Date

Abstract

Photomultiplier tubes (PMTs) play a crucial role in various research fields, particularly in particle physics, where they serve as highly sensitive detectors for light. These experiments often occur in environments with extreme radiation levels, exposing PMT components to prolonged radiation damage that can degrade their performance over time.

A critical element in the PMT structure is the dynode system, which facilitates signal amplification through the secondary electron yield (SEY) mechanism. SEY is fundamental to enhancing the initial photoelectron signal, making it essential to the detection process. Therefore, materials used for dynodes must not only exhibit a high SEY but also possess significant radiation hardness to ensure long-term stability and minimize frequent replacements.

In this study, Aluminum Oxide (Al_2O_3) and Magnesium Oxide (MgO) were selected for evaluation based on their potential to meet these criteria. The materials were subjected to controlled gamma irradiation from a Co-60 source at varying doses. Theoretical Monte Carlo simulations were conducted to assess the radiation damage in terms of displacements per atom (DPA), while SEY measurements were performed post-irradiation to quantify the impact of the radiation exposure on the SEY of the Al_2O_3 and MgO samples.

SEY measurements were conducted at the 6 MeV Tandem Accelerator at the iThemba Laboratory for Accelerator-Based Sciences (LABS) in Johannesburg. The existing microprobe setup was adapted to enable electronic measurements of SEY from MgO and Al_2O_3 samples across different radiation doses. These adaptations allowed for precise quantification of SEY variations as a function of absorbed gamma radiation dose.

The results indicate a clear inverse relationship between radiation dose and SEY: as the radiation dose increases, SEY decreases. This degradation is attributed to ionizing events induced by gamma rays, leading to the formation of vacancies and interstitial defects within the material. These structural defects alter the electronic properties of

the dynodes, ultimately reducing their amplification efficiency (SEY).

This study provides valuable insights into the radiation tolerance of dynode materials and highlights the importance of selecting robust materials to enhance the longevity and reliability of PMTs in radiation harsh environments.

Acknowledgements

I am deeply grateful to my supervisor, Prof. Elias Sideras-Haddad, for his exceptional guidance and the depth of understanding he has imparted. His influence extends beyond physics, offering perspectives that have enriched both my academic growth and personal development. I also sincerely appreciate Dr. Othmane Mouane for his steadfast support and significant contributions to this work.

To my friends, Neelan and Senkhosi, your companionship and encouragement have made this journey far more meaningful. To all my other friends, I truly appreciate the motivation and positivity you have shared along the way.

To my mother, father, and stepfather, your unwavering support, patience, and care have been invaluable. My extended family has played a vital role in shaping who I am today, and I remain profoundly thankful.

To my fiancée, Brittany, your love, patience, and encouragement have been a cornerstone of this experience. Your presence has provided strength and stability throughout, and I am deeply appreciative of the impact you have had on both my academic work and personal journey.

Contents

Declaration ii

Abstract iii

Acknowledgements v

1 Introduction 1

1.1 PMT Fundamentals . . . 2

1.1.1 Quantum Efficiency . . . 2

1.1.2 Secondary Electron Emission . . . 3

1.1.3 Radiation Harsh Environments . . . 4

1.1.4 ATLAS Detector . . . 4

1.2 Aims and Objectives . . . 7

2 Interactions of Radiation With Matter 8

2.1 Interactions of Protons With Matter . . . 8

2.1.1 Atomic Excitations . . . 8

2.1.2 Ionisation . . . 9

2.2 Interactions of Electrons With Matter . . . 9

2.2.1 Bremsstrahlung Radiation . . . 10

2.3 Interactions of Photons With Matter . . . 11

2.3.1 The Photoelectric Effect . . . 11

2.3.2 Compton Scattering . . . 12

2.3.3 Pair Production . . . 13

2.4 Interactions of Neutrons With Matter . . . 14

2.4.1 Elastic Scattering . . . 14

2.4.2 Inelastic Scattering . . . 15

2.4.3 Radiative Neutron Capture . . . 15

3 Choice Of Materials And Sample Preparation 17

3.1 Key Material Characteristics for Dynode Applications 17
3.2 List of Materials To Be Used: 20
3.2.1 Magnesium Oxide: 20
3.2.2 Aluminium Oxide: 20
3.3 Sample Preparation 20

4 Experimental Setup for Electron Emission Yield Measurements 24
4.1 Decay of Cobalt-60 26
4.2 Cobalt-60 Facility 28
4.2.1 SEY Experimental Background 31
4.3 Experimental Procedure 32

5 Results and Discussion 39
5.1 Radiation Damage and Absorbed Dose Simulations 39
5.1.1 FLUKA 39
5.1.2 Simulations 39
5.1.3 Geometries and Setup 41
5.1.4 Simulation Results 47
5.2 Offset Correction 52
5.3 Current Measurements as a Function of Dose 53
5.3.1 Magnesium Oxide 54
5.3.2 Aluminium Oxide 56
5.4 Averaged Current Measurements as a Function of Dose 58
5.4.1 Magnesium Oxide 59
5.4.2 Aluminium Oxide 59
5.4.3 Electron Emission Yield Measurements 60

6 Conclusion 67
6.1 Conclusions 67
6.2 Future Work 68

List of Tables

4.1 Irradiation conditions for different sample groups exposed to the Cobalt-60 source 30

5.1 Time-Averaged Current Measurements 58
5.2 Electron Yield Measurements 61

6.1 EEY as a function of their pristine samples EEY 68

List of Figures

1.1 Photomultiplier tube. 4
1.2 Response down-drift of innermost tiles in the ATLAS TileCal [11]. This figure shows the response of a PMT relative to the total integrated delivered luminosity. This figure demonstrates the down-drift of a PMT in a radiation-harsh environment. 6
1.3 Response variation in the PMTs used in the TileCal. 6

2.1 Compton Scattering process. 12
2.2 The following gamma-ray spectroscopy measurement displays a phenomenon known as the Compton Edge [18], this feature is due to the fact that the photons in this region have been scattered off of the atomic electrons of the target. This edge represents the maximum energy transfer that an incident photon can impart onto an atomic electron in a single scattering event. 13
2.3 Pair production process. 14
2.4 Incident neutron with energy E_n elastically scattering off of the target nucleus, the result of this interaction is the recoiling of the target nucleus with an energy E_R. deflected by angle θ and the scattered neutron with energy E_n' [13]. 15

3.1 Energy band diagrams, (a) Positive EA (b) Negative EA [24]. 19
3.2 The Specac atlas manual 15t hydraulic press. 20

4.1 Calorimeter section of the ATLAS Detector [33]. In this figure η represents the pseudorapidity which expresses the range of a section of the detector with respect to the axis of colliding beams [34]. 24
4.2 Radiation levels which the electronics found in the calorimeter systems in the ATLAS detector are subjected to [8]. Here FE crates are the "Front-End" crates which house readout electronics and LVPS refers to the "Low Voltage Power Supplies". 25

4.3 Total ionizing dose and characteristic particle fluences, obtained from GEANT4 simulations for the electronic systems shown in Figure 4.2 [8]. 25
4.4 This figure illustrates the decay pathway of Cobalt-60 ($^{60}_{27}$Co) to the ground state of Nickel-60 ($^{60}_{28}$Ni). This image illustrates the two possible decay pathways (given by the two red lines) and the energies of the electrons emitted for both possible pathways as well as the energies of the gamma-rays emitted at each stage [39]. 28
4.5 A 3D-printed sample holder was used to contain all the samples for this study. The holder was made from polylactic acid (PLA), and three such holders were printed to accommodate the samples at the three different dose levels. 29
4.6 A calibrated cylindrical ionization chamber probe, Farmer-type, which measures radiation levels, is positioned at the location where the sample holder will be placed. This probe serves as the primary reference for quantifying the dose or activity arriving from the source at that specific distance. The probe is connected to a data acquisition system, as shown in Figure 4.8. 29
4.7 Window of the Cobalt-60 source (approximately 20 cm away from the source), along with the samples designated to receive 100 kGy, housed in one of the sample holders. 30
4.8 The dose reading was taken by a probe located approximately 88 cm away from the Cobalt-60 source. This is the region where the samples designated to receive 5 kGy were housed in the sample holder. 31
4.9 6 MV Tandem Accelerator located at the iThemba LABS, Johannesburg. 32
4.10 Microprobe Carousel Setup: Showing the Teflon aperture, brass cage, and a fluorescent ceramic. 33
4.11 The microprobe chamber control interface is used for all microprobe chamber-related processes, such as vacuum pumping, venting, and other operational controls. 33
4.12 Experimental setup used to determine the EEY of the MgO and Al_2O_3 samples. 34
4.13 Al_2O_3 sample mounted on a metallic disc using graphite-based conductive paste, with a temporary rubber adhesive securing the brass cage over the sample. 35
4.14 Data Acquisition Setup. 37

5.1 Simulated absorbed dose from a mono-energetic photon source (1.25 MeV) placed 88.00 cm $\pm$ 0.05cm away from the target for 6.846 $\pm$ 0.00001 days for the two samples. 43

5.2 Simulated absorbed dose from a mono-energetic photon source (1.25 MeV) placed at a distance of 80.00 cm ± 0.05 cm from the target for 10.825 ± 0.00001 days and then placed at 20.00 ± 0.05cm from the target for 3.919 ± 0.00001 days for the two samples. 44
5.3 Simulated absorbed dose from a mono-energetic photon source (1.25 MeV) placed at a distance of 20.00 cm ± 0.05 cm from the target for 10.828 ± 0.00001 days for the two samples. 44
5.4 Simulated DPA from a mono-energetic photon source (1.25 MeV) placed 88.00 cm ± 0.05cm away from the target for 6.846 ± 0.00001 days for the two samples. Please note the scaling factor shown in the top left corner of the plot, and keep this in mind throughout the remainder of this thesis. 45
5.5 Simulated DPA from a mono-energetic photon source (1.25 MeV) placed at a distance of 80.00 cm ± 0.05 cm from the target for 10.825 ± 0.00001 days and then placed at 20.00 ± 0.05cm from the target for 3.919 ± 0.00001 days for the two samples. 45
5.6 Simulated DPA from a mono-energetic photon source (1.25 MeV) placed at a distance of 20.00 cm ± 0.05 cm from the target for 10.828 ± 0.00001 days for the two samples. 46
5.7 Simulated absorbed dose from a 70 TBq Co-60 source placed 88.00 cm ± 0.05cm away from the target for 6.846 ± 0.00001 days for the two samples. 47
5.8 Simulated absorbed dose from a 70 TBq Co-60 source placed at a distance of 80.00 cm ± 0.05 cm from the target for 10.825 ± 0.00001 days and then placed at 20.00 ± 0.05cm from the target for 3.919 ± 0.00001 days for the two samples. 48
5.9 Simulated absorbed dose from a 70 TBq Co-60 source placed at a distance of 20.00 cm ± 0.05 cm from the target for 10.828 ± 0.00001 days for the two samples. 48
5.10 Simulated DPA from a 70 TBq Co-60 source placed 88.00 cm ± 0.05cm away from the source for 6.846 ± 0.00001 days for the two samples. . . . 49
5.11 Simulated DPA from a 70 TBq Co-60 source placed at a distance of 80.00 cm ± 0.05 cm from the source for 10.825 ± 0.00001 days and then placed at 20.00 ± 0.05cm from the source for 3.919 ± 0.00001 days for the two samples. 49
5.12 Simulated DPA from a 70 TBq Co-60 source placed at a distance of 20.00 cm ± 0.05 cm for 10.828 ± 0.00001 days for the two samples. 50

5.13 This figure serves as a reference for the normalized dose (Gy) distribution of a 10 MeV electron beam, exhibiting characteristics similar to those observed in the final simulations presented above [49]. Although the material densities used in the referenced figure are higher than those employed in this study, the figure is included to demonstrate the simulation's ability to reproduce experimental trends. 51
5.14 Current Vs Time measurements for the Al_2O_3 Pristine sample, including both the negative and positive bias and their respective offset measurements included. 52
5.15 Measured current under positive and negative applied voltage bias for pristine Magnesium Oxide. 54
5.16 Measured current under positive and negative applied voltage bias for Magnesium Oxide samples with an absorbed gamma radiation dose of 5 kGy. 54
5.17 Measured current under positive and negative applied voltage bias for Magnesium Oxide samples with an absorbed gamma radiation dose of 50 kGy. 55
5.18 Measured current under positive and negative applied voltage bias for Magnesium Oxide samples with an absorbed gamma radiation dose of 100 kGy. 55
5.19 Measured current under positive and negative applied voltage bias for pristine Aluminium Oxide. 56
5.20 Measured current under positive and negative applied voltage bias for Aluminium Oxide samples with an absorbed gamma radiation dose of 5 kGy. 56
5.21 Measured current under positive and negative applied voltage bias for Aluminium Oxide samples with an absorbed gamma radiation dose of 50 kGy. 57
5.22 Measured current under positive and negative applied voltage bias for Aluminium Oxide samples with an absorbed gamma radiation dose of 100 kGy. 57
5.23 Averaged measured current under positive and negative applied bias for Magnesium Oxide samples as a function of absorbed gamma radiation dose. 59
5.24 Averaged measured current under positive and negative applied bias for Aluminium Oxide samples as a function of absorbed gamma radiation dose. 59

5.25 This figure presents the variation in electron emission yield of Aluminium Oxide as a function of radiation dose, illustrating how the material's electron emission yield responds to increasing gamma radiation exposure. 61
5.26 This figure presents the variation in electron emission yield of Magnesium Oxide as a function of radiation dose, illustrating how the material's electron emission yield responds to increasing gamma radiation exposure. 62
5.27 This figure presents the combined variation in electron emission yield of both Magnesium Oxide and Aluminium Oxide as a function of radiation dose, illustrating how the material's electron emission yield responds to increasing gamma radiation exposure. 63
5.28 Secondary electron yield as a function of the primary electron energy for Aluminium Oxide and Magnesium Oxide thin films at varying film thickness [52]. 64
5.29 Normalized electron emission yield for a Copper sample at varying levels of absorbed radiation dose induced by photons [53]. 64
5.30 SEY as a function of the absorbed electron dose on a copper sample, based on [54], for an electron energy of 500 eV (dark gray) and 10 eV (gray). 66

Chapter 1

Introduction

In July 2012, both of the two general-purpose particle detectors at the European Organization for Nuclear Research (CERN), namely, the ATLAS and CMS collaborations, reported excesses of events in their 2011 datasets of proton-proton collisions. The centre-of-mass energy of these excess events was $\sqrt{s} = 7$ MeV, which was in the theoretical range of standard model Higgs boson production and decay in the mass region 124-126 GeV [1]. This revolutionary measurement was the final piece of the puzzle when it came to completing the standard model of particle physics.

Discoveries such as the Higgs boson underpin the importance of the electronic systems present within particle physics detectors, this emphasizes the importance and need of preserving these electronic components of detectors such as the ATLAS. One of these electrical components are the PMTs which are usually placed at the epicenter of these experiments. At the heart of these huge experiments (the interaction points) the levels of radiation are extremely high, for example, during the high luminosity LHC (HL-LHC) runs planned to begin after 2030, the upgraded inner tracker upgrade (ITk) sensors of the ATLAS pixel detector are expected to accumulate in excess of 10^{16} 1 MeV n_{eq}/cm^2 (that is to say 10^{16} 1 MeV neutron equivalent particles per squared centimeter) [2].

It stands to reason that electronics placed in detectors such as the ATLAS detector are exposed to extreme levels of radiation, as such the performance of the electronics decays as a function of the amount of radiation they are exposed to. During the period of the LHC Run 1, spanning the years 2011 & 2012 the radiation-induced damage to the electronics of the LHC was the primary source of accelerator downtime [3].

The photomultiplier tube (PMT) is one of the most significant electronic instruments in physics experiments today. By amplifying photocurrents, PMTs play a crucial role in detecting particles (single-photon counting) and enabling researchers to study their

physical properties in detail, thereby advancing our understanding of the fundamental aspects of nature.

Since then, PMTs have become ubiquitous in experimental physics, with applications spanning a multitude of fields. A prominent example is particle physics, where PMTs are essential for detecting particles and measuring their properties, a role that frequently intersects with nuclear physics research. Among particle physics experiments, the most notable is the Large Hadron Collider (LHC) at CERN.

PMTs operate in extremely radiation-harsh environments. In particle and nuclear physics experiments, electronics are exposed to a wide range of radiation, including photons, neutrons, and ions. Each of these particles interacts with matter differently, depending on properties such as charge and energy. However, all of them contribute to radiation damage, gradually degrading materials and leading to electronic fatigue. Over time, this degradation results in a decline in overall performance, impacting the longevity and reliability of these systems.

1.1 PMT Fundamentals

1.1.1 Quantum Efficiency

PMTs are typically devices that are comprised of an evacuated glass housing unit, which contains a photocathode as well as an anode. As mentioned in the introduction of this work, the PMT has been used in physics experiments since the 1930's, as such they have been optimised and perfected over the course of their existence. The quantum efficiency of a photodetector can be described as follows:

When ionising radiation interacts with a scintillating material, it results in the emission of photons, which are subsequently detected by photomultiplier tubes (PMTs). The photons strike the photocathode of the PMT, and if their energy exceeds the work function of the material, they transfer this energy to electrons within the photocathode, resulting in the emission of electrons. This process, known as the photoelectric effect, is governed by the following equation:

$$E = h\nu - E_b \tag{1.1}$$

Where E is the energy imparted to the electron, h is Planck's constant, ν is the frequency of the light and E_b is the work function of the photocathode (this will be explained in further detail). This equation relates how an electron in the photocathode is excited from the conduction band into the vacuum of the PMT. Not all photons

are converted into photoelectrons. To determine the quantum efficiency involved in the interaction first the radiant sensitivity must be derived (the photoelectric current divided by the incident radiant flux [4]). The radiant sensitivity is characterised by the following equation:

$$Sk = \frac{I_k}{L_p} \tag{1.2}$$

Where I_k is given by the is the photocurrent of the PMT and L_p is the incident radiant flux at the wavelength of interest [4]. Once the radiant sensitivity is known the quantum efficiency can be determined using the following relation:

$$\eta = \frac{h \cdot c}{\lambda \cdot e} \cdot Sk \tag{1.3}$$

Where η is the quantum efficiency, λ is the wavelength of the incident light, c is the speed of light and e is the fundamental charge of the electron [4]. The quantum efficiency of a PMT is one important characteristic of the working mechanics of the PMT.

1.1.2 Secondary Electron Emission

Quantum efficiency is a fundamental aspect of a photomultiplier tube (PMT), but the true power of a PMT lies in its ability to amplify the initial signal to a measurable level. When a photoelectron is generated at the photocathode, it is directed toward the first dynode. A PMT contains several dynodes, each at a progressively higher electrical potential. Dynodes are typically made of, or coated with, materials that have a low work function [5]. As the primary electrons from the photocathode, or secondary electrons from previous dynodes, strike the dynodes, secondary electrons are emitted due to the low work function. With each successive dynode having a higher electrical potential, the number of secondary electrons produced increases between successive dynodes, creating a cascade effect that significantly amplifies the original signal.

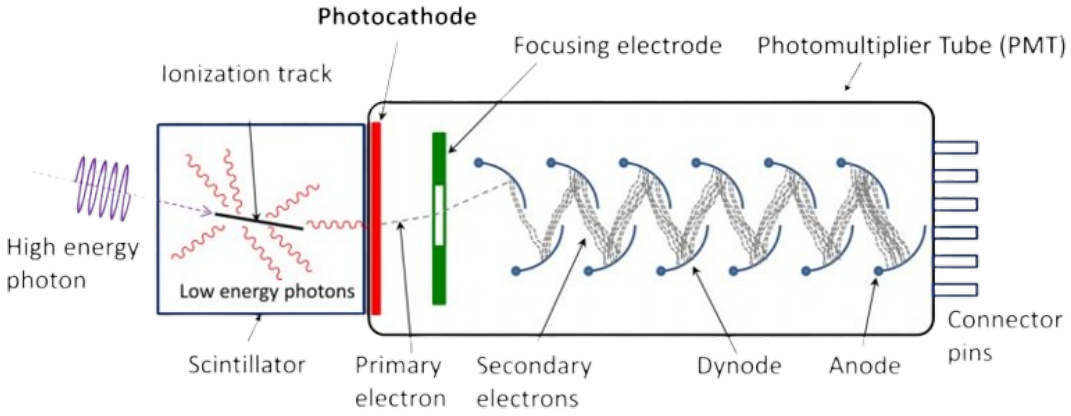


Figure 1.1: Photomultiplier tube.

Figure 1.1 illustrates the process of an incident photon striking the photocathode, where its energy is subsequently transferred to an electron in the photocathode, resulting in the emission of a photoelectron. The figure then shows the subsequent amplification of this electron as it travels through the series of dynodes, where secondary electron emission occurs and increases at each stage due to the increasing electrical potential. This cascade effect continues until the electron reaches the anode, where the amplified signal is then directed through the connector pins for measurement and further processing. Figure extracted from [6].

1.1.3 Radiation Harsh Environments

Experiments in experimental physics often involve the production and study of intense radiation, utilizing electronic devices like PMTs to measure various phenomena. Due to the extreme radiation environments, these electronic components are expected to deteriorate over time.

Physics experiments frequently push these components to their limits. For instance, the KM3NeT experiment which plans to employ over 6,000 photodetection modules, each containing 31 PMTs [7]. This is just one example among many that highlight the widespread use of PMTs in experimental physics.

Radiation harsh environments and high energy physics measurements are ubiquitous with one another, thus the need for radiation-hard electronics is of great importance.

1.1.4 ATLAS Detector

The ATLAS detector, and specifically the ATLAS Tile Hadron Calorimeter (TileCal), generates a vast amount of data regarding the health and performance of its PMTs.

This section will emphasize the importance of PMTs and their radiation hardness. Located at the heart of the ATLAS experiment at the LHC, TileCal exemplifies the crucial role PMTs play in particle physics. The entire ATLAS detector stands 25 meters tall, extends 44 meters in length, and weighs approximately 7,000 tons [8]. TileCal is a sampling calorimeter that uses iron plates as the absorber material and plastic scintillating tiles as the active material (The material that emits photons when energy is deposited by charged particles interacting with it) [9]. When charged particles pass through the calorimeter, they produce scintillation light in the tiles. This light is then carried by wavelength-shifting optical fibers to approximately 10,000 PMTs, where it is detected and analyzed [9].

The LHC has four main interaction points: the locations in the LHC where the proton or heavy ion beams collide at extremely high energies. During proton-proton (pp) collisions the energy at interaction is 13.6 TeV [1]. During these interactions decay products produced by pp collisions are created, these products as well as the initial protons eventually interact with the surrounding matter [10]. The high energies of the decay products and the initial protons create an extremely harsh radiation environment for the surrounding matter (including PMTs).

Due to the harsh radiation environments present at particle detectors such as the ATLAS experiment, the electronics (particularly those closest to the epicenter of collisions) responsible for particle detection decay with time. The TileCal undergoes various response measurements such as the Laser calibration system which measures the response variation of a PMT relative to the day the PMT was installed [11]. The "down-drift" of PMT response, shown by measurements such as the Laser calibration system finds that PMTs in radiation harsh environments such as the ATLAS detector exhibit an exponential decay in performance [11].

The main parameter that can be used to measure the decay of response of a PMT is known as the gain. The gain of a PMT refers to the multiplication factor by which the initial number of photoelectrons generated at the photocathode is increased as they cascade through the dynodes (this will be more clearly outlined in section 3.3). The loss of gain of a PMT is indicative of the degree of radiation damage the PMT has undergone. If a PMT has n dynodes with an average electron gain of N per dynode, the overall gain [5] is given by:

$$G = N^n \tag{1.4}$$

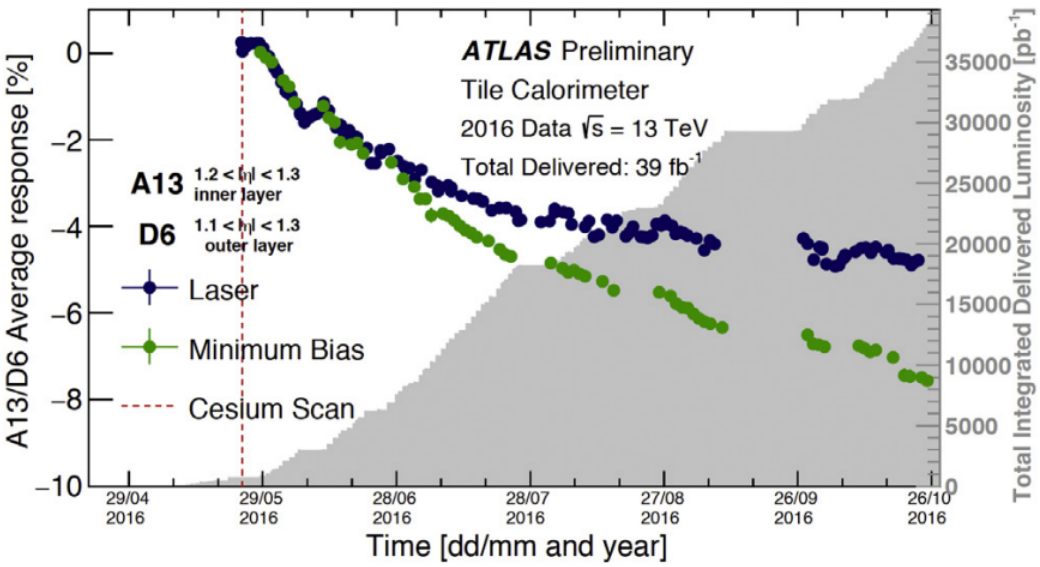
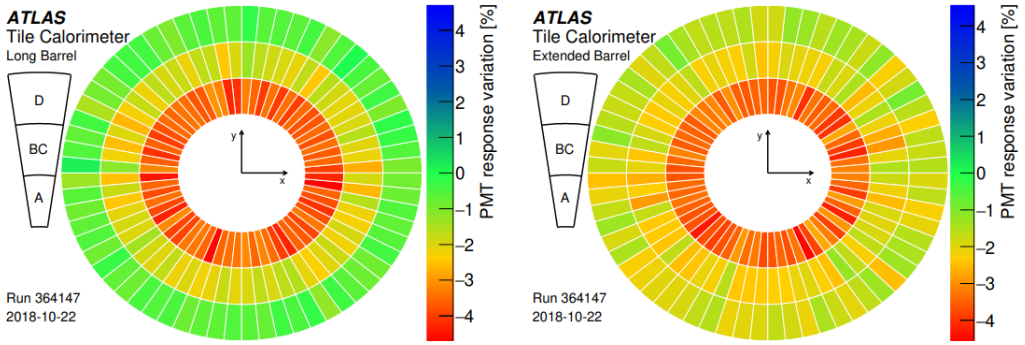


Figure 1.2: Response down-drift of innermost tiles in the ATLAS TileCal [11]. This figure shows the response of a PMT relative to the total integrated delivered luminosity. This figure demonstrates the down-drift of a PMT in a radiation-harsh environment.



(a) (b)

Figure 1.3: Response variation in the PMTs used in the TileCal.

Figure 1.3 demonstrates the mean response variation in the PMTs for both the TileCals Long Barrel and the TileCals extended barrier. This figure was generated using the entire dataset generated by pp collisions during the 2018 data-taking period [12]. The innermost PMTs of the ATLAS TileCal experience the greatest loss in response variation (gain). This is due to the fact that these PMTs are closest to the interaction point and demonstrate the relationship between the decay of variation and the absorbed dose of the PMT.

1.2 Aims and Objectives

Photomultiplier tubes (PMTs) play a crucial role in particle physics experiments. However, these experiments often involve extremely high levels of radiation, which can significantly degrade the performance of electronic systems, including PMTs. This study examines how radiation exposure impacts the materials used in the construction of a PMT, with a specific focus on the dynodes. Dynodes are critical components of a PMT, responsible for amplifying the photocurrent by secondary electron emission. Specifically, it examines how the electron emission efficiency of the dynodes diminishes as a function of the radiation dose, as detailed further in Chapter 3.

Below is a list of questions that forms the basis of this study:

- How does the interaction of radiation with matter influence the properties of materials?
- In what ways does the interaction of radiation with matter impact electronic components?
- How does the interaction of radiation with matter affect the electron emission properties of a PMT dynode and the materials commonly used in its construction?

Chapter 2

Interactions of Radiation With Matter

All particles present in high-energy physics experiments, whether they are primary particles or decay products resulting from their interactions, will eventually interact with the surrounding matter [10]. Understanding these interactions is crucial for interpreting experimental results, optimizing detector performance, and assessing the effects of radiation on materials in the form of defects. In this section, the interaction of various particles with matter will be outlined.

2.1 Interactions of Protons With Matter

Protons are subatomic particles that belong to a family of particles known as hadrons. Hadrons are composed of 2 up quarks and a down quark. The up quark has a charge of $+\frac{2}{3}e$, with the down quark having a charge of $-\frac{1}{3}e$ amounting to the total charge of the proton: $+1e$. Since the proton has a positive charge and is relatively massive (m_p = 1.67262192 $\cdot$ 10^{-27} kg) it experiences both atomic interactions, mediated through the electromagnetic force, as well as interactions mediated by the strong force.

2.1.1 Atomic Excitations

Due to the charged nature of protons, they interact primarily through Coulomb forces with the orbital electrons of the target atom [13]. Depending on the magnitude of the energy imparted by the proton to the target atom, the interaction can result in atomic excitations. Atomic excitations occur when a charged particle interacts with the target atom and provides sufficient energy to promote one of the atom's electrons to a higher energy state (shell) [14]. The excitation of an atom leads to the atom being in an

unstable state, which causes the atom to de-excite by emitting a low-energy ultraviolet photon.

2.1.2 Ionisation

When a proton traverses a material medium, it primarily interacts with the electrons bound to the atoms of the target. If the energy transferred from the proton to a bound electron exceeds the ionisation potential of the atom, defined as the minimum energy required to liberate the electron, the atom becomes ionised:

$$E_{proton} \geq E_{Ionisation} \tag{2.1}$$

The ionisation of an atom leads to an ion pair, that being the electron that has been stripped away from the atom (secondary electron) and the atom that now has a vacancy in one of its electron shells. If the secondary electron which forms a part of the ion pair has sufficient energy to cause further ionisation, this secondary electron is known as a delta ray [14].

As protons traverse materials, energy loss occurs due to the transfer of the protons' energy to target atoms. This energy loss is described by the Bethe-Bloch formula, which quantifies the mean energy loss per unit distance traveled through the material [15]:

$$-\frac{dE}{dx} = 2\pi N_a {r_e}^2 m_e c^2 \rho \frac{Z}{A}\frac{z^2}{\beta^2}\left[ln\left(\frac{2m_e\gamma^2\nu^2 W_{max}}{I^2}\right) - 2\beta^2 - \delta - 2\frac{C}{Z}\right] \tag{2.2}$$

The parameters of Equation 2.2 are well established in the literature of high-energy physics [15].

2.2 Interactions of Electrons With Matter

The mass of the electron ($m_p = 9.1093837 \cdot 10^{-31}$ kg) is roughly 2000 times less smaller than the mass of the proton. If an electron and a proton have the same momentum, the electron will have a significantly higher velocity. In addition to the energy transfer mechanisms that protons undergo when interacting with a material, electrons also experience another energy loss mechanism due to their small mass: bremsstrahlung radiation [15]. This occurs alongside the energy loss processes common to both protons and electrons. Thus the total energy loss of an electron can be expressed by the following formula:

$$\left(\frac{dE}{dx}\right)_{tot} = \left(\frac{dE}{dx}\right)_{rad} + \left(\frac{dE}{dx}\right)_{coll} \tag{2.3}$$

Where the subscripts correspond to the total energy loss, the energy loss caused by radiation (Bremsstrahlung) and coll which is the energy loss caused by collisional interactions of the electron with the target atom.

2.2.1 Bremsstrahlung Radiation

Bremsstrahlung radiation occurs when a charged particle, most notably an electron, is decelerated as it moves through a target material. This energy loss results from various scattering events, as discussed earlier. If a charged particle—specifically an electron in this context—has energy much greater than its rest energy ($E_{rest} = E_0 = m_o c^2$), where m_0 is the rest mass, it will emit bremsstrahlung radiation as it traverses the material [16].

As electrons traverse through a material, they are attracted to the positively charged nuclei of the material and are decelerated and deflected by Coulombic interactions, this lost energy which accounts for the deceleration of the electron is emitted in the form of a low energy photon - this process is known as Bremsstrahlung radiation.

If an electron is accelerated through a potential V, the maximum energy the electron can reach is given by [16]:

$$E_{max} = eV \tag{2.4}$$

Where e is the unit electronic charge. The maximum energy of the Bremsstrahlung radiation released from this electron will then also be equal to eV:

$$E_{brems} \leq E_{max} = eV \tag{2.5}$$

Since Bremsstrahlung radiation is photonic, equation 2.8 can be rewritten in the form:

$$h\frac{c}{\lambda} \leq eV \implies \lambda \geq \frac{hc}{eV} \tag{2.6}$$

Where h is Planck's constant and c is the speed of light. The minimum wavelength (λ_{min} - cutoff wavelength for Bremsstrahlung radiation) that will be emitted from the Bremsstrahlung process is therefore:

$$\lambda_{min} = \frac{hc}{eV} \tag{2.7}$$

2.3 Interactions of Photons With Matter

Photons are charge-less elementary particles of light and electromagnetic radiation. Since photons are charge-less their interactions are different from their charged counterparts. The main mechanisms for photonic interactions with matter are:

2.3.1 The Photoelectric Effect

The photoelectric effect occurs when an incident photon is completely absorbed by an atom, resulting in the ejection of one of its bound electrons. In this process, the entire atom, including its electron cloud, absorbs the photon energy. The photon transfers its energy to an inner-shell electron, which is then emitted from the atom if the photon's energy exceeds the electron's binding energy. The kinetic energy E of the ejected photoelectron is given by [15]:

$$E = h\nu - B.E. \tag{2.8}$$

- E is the kinetic energy of the emitted photoelectron
- $h\nu$ is the energy of the incident photon
- $B.E.$ is the binding energy of the electron within the atom

After the photoelectron is ejected, the atom is left in an excited state due to the inner-shell vacancy. This vacancy is typically filled by an electron from a higher energy shell, and the excess energy from this transition is released either as characteristic X-ray photons or transferred to another electron, which is then emitted as an Auger electron.

The recoil momentum from the ejected photoelectron is absorbed by the much heavier nucleus, preserving conservation of momentum. This explains why the photoelectric effect cannot occur with free electrons — doing so would violate energy and momentum conservation laws.

The probability of the photoelectric effect occurring is highest at low photon energies, particularly below 0.1 MeV, and increases sharply with atomic number Z, making it more probable in materials with high atomic number.

2.3.2 Compton Scattering

Compton scattering is caused by the scattering of photons off of free electrons. With regards to the interactions of radiation with matter, these electrons will be bound to atoms, however, if the photon energy is far greater than the binding energy of the electron ($E_{photon} \gg B.E._{electron}$) the electron can be approximately treated as a free electron [15].

Equation 2.9 is known as the Compton equation and describes how the wavelength of the incident photon changes due to the interaction of the incident photon and the free electron which leads to the energy loss of the incident photon.

$$\lambda_2 - \lambda_1 = \frac{h(1 - \cos(\theta))}{mc} \tag{2.9}$$

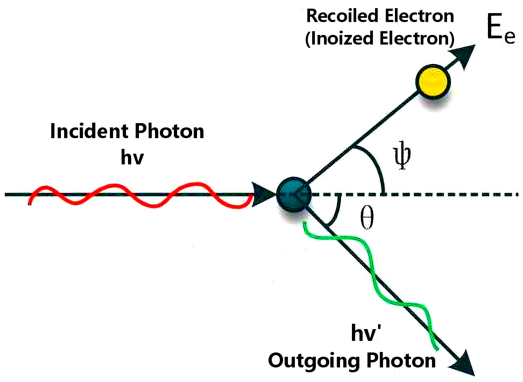


Figure 2.1: Compton Scattering process.

Figure 2.1 illustrates how an incident photon interacts with an atomic electron, transferring energy to it. As a result, the electron is ejected from the atom, and the photon loses energy and is deflected from its original path [17].

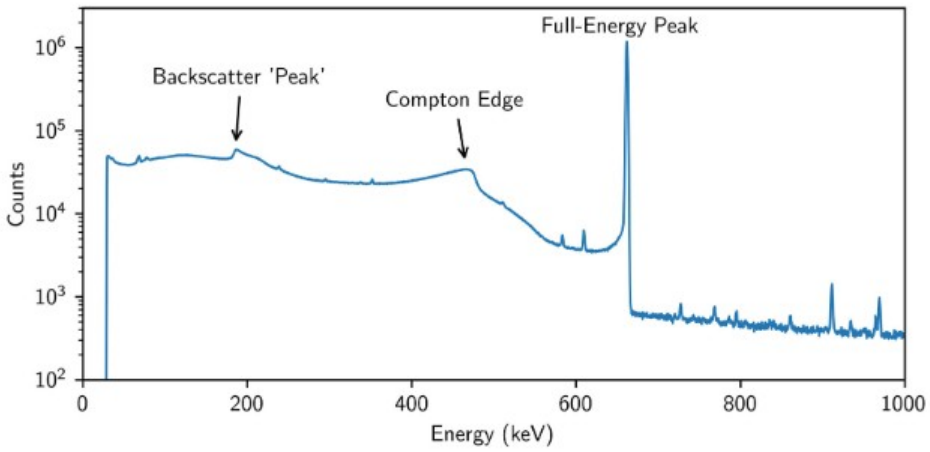


Figure 2.2: The following gamma-ray spectroscopy measurement displays a phenomenon known as the Compton Edge [18], this feature is due to the fact that the photons in this region have been scattered off of the atomic electrons of the target. This edge represents the maximum energy transfer that an incident photon can impart onto an atomic electron in a single scattering event.

2.3.3 Pair Production

Pair production is the process in which a photon is transformed into an electron-positron pair. In order for the conservation of momentum and energy to not be violated pair production is only possible in the presence of a third body which is usually a nucleus [15]. The minimum energy of the photon required for pair production is tied to the rest energy of the particles being created. An electron and a positron each have a rest mass of about 0.511 MeV/c^2. So, the total rest energy for the pair is:

$$2 \cdot 0.511 MeV = 1.022 MeV \tag{2.10}$$

The pair production process is represented by the following equation [16]:

$$\gamma + X \rightarrow e^- + e^+ + X^* \tag{2.11}$$

- γ denotes the incident photon
- X and X^* represent the ground state and excited state of the nucleus, respectively
- and e^- and e^+ signify the electron and positron, respectively

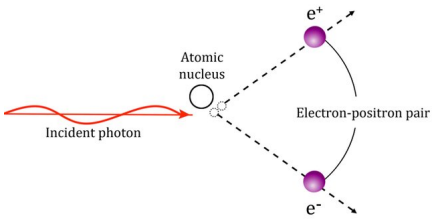


Figure 2.3: Pair production process.

Figure 2.3 depicts the pair production process, in which an incident photon interacts with an atomic electron which results in the transformation of the incident photon and atomic electron into an electron-positron pair.

2.4 Interactions of Neutrons With Matter

The neutron is a subatomic particle that like the photon belongs to the group of families known as hadrons and as such is comprised of 3 quarks. Unlike the proton the neutron is comprised of 1 up quark and 2 down quarks, which implies the charge of the neutron much like its namesake is neutral ($1\cdot+\frac{2}{3}e+2\cdot-\frac{1}{3}e$). The neutron much like the proton is relatively massive ($m_n = 1.674927471 \cdot 10^{-27}$), however due to the charge neutrality of the neutron it is not subject to Coulombic interactions and only partakes in interactions with atomic nuclei, mediated by the strong force.

The main mechanisms which characterise the interactions of neutrons with matter are described in the sections below:

2.4.1 Elastic Scattering

Similar to the elastic scattering described earlier, the elastic scattering of a neutron with a nucleus follows a comparable process. In this interaction, a neutron transfers a portion of its energy to the atomic nucleus, causing the incident neutron to deflect and the nucleus to recoil. This mechanism is most probable for high-velocity neutrons interacting with atomic nuclei with a low atomic number [19].

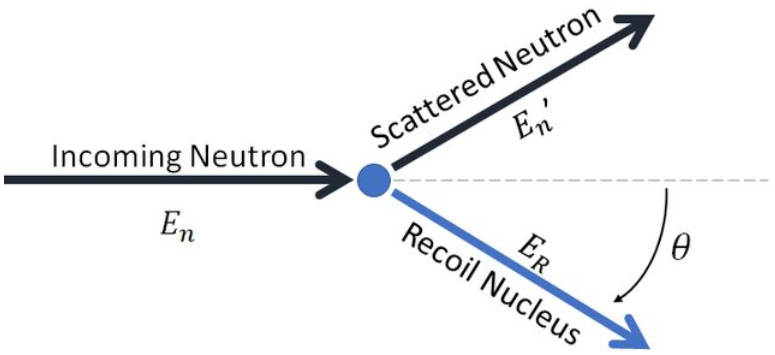


Figure 2.4: Incident neutron with energy E_n elastically scattering off of the target nucleus, the result of this interaction is the recoiling of the target nucleus with an energy E_R. deflected by angle θ and the scattered neutron with energy E_n' [13].

2.4.2 Inelastic Scattering

In an inelastic scattering process, the incident neutron interacts with an atomic nucleus, leaving the atomic nucleus in an excited state. This excited atomic nucleus can de-excite by the emission of a gamma-ray or another form of radiative emission [15]. For an inelastic collision to occur, the incident neutron must have an energy sufficient enough to excite the atomic nucleus. This energy is of the order of 1 MeV, if the incident neutron has an energy less than 1 MeV, only elastic scattering can occur.

2.4.3 Radiative Neutron Capture

Radiative neutron capture is the process in which an incident neutron is 'captured' by a target atomic nucleus. The cross-section for neutron capture is approximately given by:

$$\sigma = \frac{1}{v} \tag{2.12}$$

Where v is the velocity of the incident neutron and σ is the cross-section for neutron capture. It follows that radiative neutron capture is more likely at lower incident neutron energies. Radiative neutron capture results in the target nucleus being in an excited state. In order for the atomic nucleus to return to a more stable state the nucleus will typically emit one or more gamma-rays [15]. The formula that governs radiative neutron capture is given by:

$$n + {}^{A}_{Z}X \rightarrow {}^{A+1}_{Z}X^{*} \tag{2.13}$$

- n is the incident neutron

- ${}^{A}_{Z}X$ is the target atomic nucleus
- ${}^{A+1}_{Z}X^{*}$ is the target atomic nucleus which has captured the incident neutron, and is left in an excited state (denoted by the *)

Following this process the atomic nucleus is left in an excited state and therefore has to de-excite by the emission of a gamma-ray.

$$ {}^{A+1}_{Z}X^{*} \rightarrow {}^{A+1}_{Z}X + \gamma \tag{2.14} $$

Where γ represents the emitted gamma-ray, it should be noted that this γ term may denote either a single gamma-ray or multiple gamma-rays, depending on the specific context. Additionally, depending on the context, the nucleus ${}^{A+1}_{Z}X$ may undergo β decay, a process in which a neutron is converted into a proton, or a proton into a neutron, determined by whichever transformation enables the nucleus to achieve a more stable configuration.

Chapter 3

Choice Of Materials And Sample Preparation

3.1 Key Material Characteristics for Dynode Applications

Photomultiplier tubes (PMTs) operate in moderate to extremely radiation-harsh environments. Therefore, the dynode material used for signal amplification must not only have a high secondary electron yield (SEY) but also be radiation-hard [20].

When primary photons or electrons strike the dynode, they lose energy through collisions with the dynode's electrons and ions, producing secondary electrons. At higher primary electron energies, the electrons travel faster and interact less with the dynode material, allowing them to penetrate deeper into the dynode. However, secondary electrons generated deeper within the material are more likely to lose energy before reaching the surface, resulting in a reduced contribution to the overall secondary electron yield. As the primary electron interacts with the material, energy is lost during each interaction and subsequently the interaction time increases, resulting in a higher yield of secondary electrons. The result of this is that the depth of secondary electron generation is inversely proportional to the primary electron energy [20].

In the TileCal, photons generated in the plastic scintillators are transmitted to the PMTs via wavelength-shifting fiber optic cables. Upon reaching the PMTs, these photons interact with the photocathode, where the photoelectric effect results in the emission of an electron. The result of this is the acceleration of the electron toward the first dynode due to the applied voltage, causing the emission of secondary electrons. These secondary electrons are further directed toward subsequent dynodes, with each stage

experiencing a voltage gain that facilitates additional secondary electron emission. This cascading multiplication process ultimately amplifies the signal.

High-energy primary electrons generate many secondary electrons. However, many of these electrons, generated deep within the dynode, lose the majority of their energy through scattering processes during transport. As a result, not all of them escape the dynode surface [20].

Metals have a high electrical conductivity, however, despite this, they are poor electron emitters. This is because primary electrons striking a metal surface excite electrons in the conduction band, which then interact and scatter with other electrons. These secondary electrons lose energy and do not have enough energy to overcome the metal's work function, preventing them from escaping the surface [21].

Insulating materials, on the other hand, are more promising candidates for dynodes. Secondary electrons are generated when primary electrons interact with and excite valence electrons, promoting them into the conduction band. The lifetime of these secondary electrons depends on various scattering processes, such as electron-electron, electron-impurity, and electron-phonon scattering. However, because insulators have fewer conduction band electrons, secondary electrons experience fewer scattering events, allowing them to retain more energy and travel farther through the material [20].

Generally, a material that is under consideration for use as a dynode in a PMT should meet the following criteria [21]:

- High Secondary Electron Yield (SEY): The material should efficiently produce secondary electrons when struck by primary photons or electrons.
- Transport Efficiency: The material must allow generated secondary electrons to travel to the surface without significant loss of energy.
- Low Surface Barrier: The material should have a low work function to facilitate the emission of secondary electrons into a vacuum.

In addition to the criteria mentioned above, a crucial characteristic of an effective dynode material for use in a PMT is Negative Electron Affinity (NEA). Electron affinity (EA) (χ) is the energy difference between the vacuum level and an insulator's or modified metal surface's conduction-band minimum, representing the energy needed for an electron to escape the material [22]. In NEA materials, χ is negative because the conduction band lies above the vacuum level, allowing electrons to escape without an energy barrier. This enhances secondary electron production as excited electrons in the conduction band generated by external sources face minimal scattering due to the

scarcity of conduction electrons, travel farther, and exit the material efficiently [23].

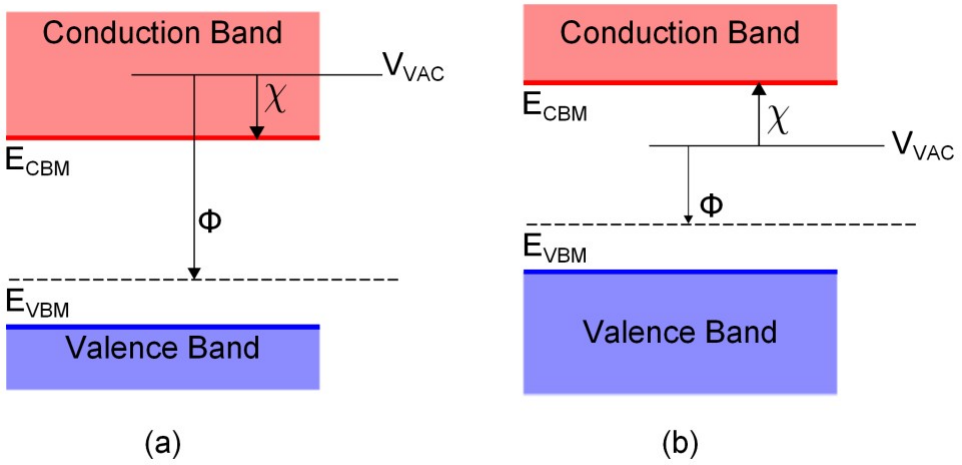


Figure 3.1: Energy band diagrams, (a) Positive EA (b) Negative EA [24].

Generally, in insulators, there are few electrons in the conduction band. This implies that fewer scatterings occur between the internally generated secondary electrons and the conduction electrons. The absence of electron-electron scattering events causes the secondary electrons to lose less energy as they move through the material, and their escape depth - the distance which a secondary electron can travel through a material whilst still maintaining sufficient energy to escape the material becomes larger [23].

Secondary electrons lose energy through two primary scattering interactions: scattering with valence electrons and scattering with atomic lattice vibrations [21].

When a secondary electron interacts with the material's valence electrons, it transfers energy, causing the valence electrons to be excited into the conduction band. However, in insulators, materials characterized by a wide band gap—secondary electrons with kinetic energy less than the band gap energy, E_{gap}, cannot participate in secondary electron-electron interactions. This limitation arises because the energy required for a secondary electron to excite a valence electron must meet or exceed E_{gap}.

Lattice vibration scattering becomes the dominant process when the secondary electron energy is below E_{gap}. In this scenario, low-energy secondary electrons transfer energy to the material's lattice, losing their own energy in the process. However, these electrons generally lack sufficient energy to escape the material [21].

3.2 List of Materials To Be Used:

3.2.1 Magnesium Oxide:

In this study MgO was selected as a candidate material a dynode could be constructed out of or coated with, the reason for this selection is as follows:

- The SEY of MgO varies in literature, typically ranging from 5 to 12 secondary electrons per incident particle [25]. This high SEY property makes MgO suitable for various applications, such as increasing the efficiency of channel electron multipliers which were found to have an improvement factor of 3 when coated with MgO [26]. MgO is also known as a moderately radiation hard material and only exhibits degradation at high doses [27].

3.2.2 Aluminium Oxide:

In this study Al_2O_3 was selected as a candidate material a dynode could be constructed out of or coated with, the reason for this selection is as follows:

- While Al_2O_3 has a relatively high secondary electron yield, typically in the range of 3 to 4 [28], it is also an excellent choice for a dynode due to the material's stability under vacuum conditions and sustained electron bombardment [29].

3.3 Sample Preparation

The Al_2O_3 and MgO powders, each with a purity of 99.9%, were commercially obtained. These materials were then pressed into pellet form.



Figure 3.2: The Specac atlas manual 15t hydraulic press.

The Al_2O_3 and MgO samples were inserted into a high-speed steel die set with a diameter of 9.23 $\pm$ 0.005 mm, with the goal of achieving a final sample thickness of 1 mm. In order to achieve this the following calculation was undertaken:

The density of the two materials:

- MgO : $\rho_0 = 3.585 \quad g/cm^3$ [30]
- Al_2O_3 : $\rho_0 = 3.99 \quad g/cm^3$ [31]

The Volume of a cylinder with radius 0.5 cm and thickness 1 mm:

$$V = \pi \cdot r^2 \cdot h \tag{3.1}$$

$$V = \pi \cdot (0.4615 \pm 0.00025\ cm)^2 \cdot (0.1\ cm) \tag{3.2}$$

Now to find the correct mass to use for each sample:

- Al_2O_3

$$\rho_0 = \frac{m}{V} \tag{3.3}$$

Where m is the required mass to achieve a cylinder with radius 0.4615 ± 0.00025 cm and thickness 1 mm.

$$V = \pi \cdot r^2 \cdot h = \pi \cdot (0.4615 \pm 0.00025\ \text{cm})^2 \cdot (0.1\ \text{cm}) \tag{3.4}$$

$$m = \rho \cdot V = 3.99\ \text{g/cm}^3 \cdot \pi \cdot (0.4615 \pm 0.00025)^2 \cdot (0.1) \tag{3.5}$$

$$m = 0.268\ \text{g} \tag{3.6}$$

Now applying error propagation:

$$\frac{\Delta m}{m} = 2 \cdot \frac{\Delta r}{r} = 2 \cdot \frac{0.00025}{0.4615} \approx 0.001084 \tag{3.7}$$

$$\Delta m = 0.268 \cdot 0.001084 \approx 0.0003\ \text{g} \tag{3.8}$$

$$m = (0.268 \pm 0.0003)\ \text{g} \tag{3.9}$$

- MgO

$$\rho_0 = \frac{m}{V} \tag{3.10}$$

$$m = 3.585\ \ \text{g/cm}^3 \cdot \pi \cdot (0.4615 \pm 0.00025)^2 \cdot (0.1\ \text{cm}) \tag{3.11}$$

$$m = 0.241\ \text{g} \tag{3.12}$$

Applying the same uncertainty propagation:

$$\frac{\Delta m}{m} = 2 \cdot \frac{\Delta r}{r} = 2 \cdot \frac{0.00025}{0.4615} \approx 0.001084 \tag{3.13}$$

$$\Delta m = 0.241 \cdot 0.001084 \approx 0.0003\ \text{g} \tag{3.14}$$

$$m = (0.241 \pm 0.0003)\ \text{g} \tag{3.15}$$

Once the masses of Al_2O_3 and MgO were determined, the powders were weighed using a scale. To prevent contamination, a sheet of paper was first placed on the scale and weighed. The scale was then zeroed, and the powders were added gradually on to the paper until the desired mass was reached. Afterward, the powders were transferred into the die set and placed in the Specac Atlas Manual 15T hydraulic press, where a force of 14 000 kg * 9.81 $m \cdot s^{-2}$ was applied, reaching a maximum pressure of:

$$P = \frac{F}{A} \tag{3.16}$$

$$P = \frac{14{,}000\ \text{kg} \times 9.81\ \text{m} \cdot \text{s}^{-2}}{\pi \cdot (0.004615)^2\ \text{m}^2} \tag{3.17}$$

$$P = 2.05 \times 10^9\ \text{N/m}^2 = 2{,}050\ \text{MPa} \tag{3.18}$$

A total of 12 samples were prepared for both Al_2O_3 and MgO. This results in three samples per material for each radiation dose, including three pristine samples and three samples for each of the three different radiation doses.

Chapter 4

Experimental Setup for Electron Emission Yield Measurements

The ATLAS detector, recognized as the largest-volume particle detector ever built [32], provides an unparalleled platform for evaluating the resilience of electronic systems under extreme radiation conditions. Within this detector, the TileCal stands out as an optimal candidate for benchmarking the radiation levels experienced by PMTs, given the numerous PMTs deployed in an extremely high-radiation environment.

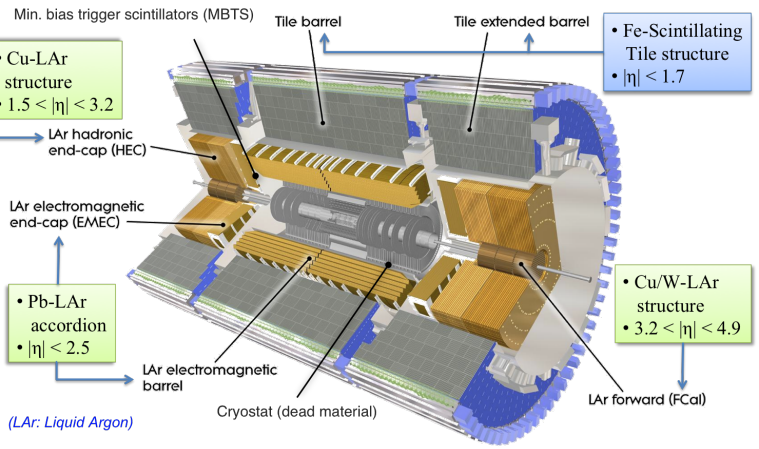


Figure 4.1: Calorimeter section of the ATLAS Detector [33]. In this figure η represents the pseudorapidity which expresses the range of a section of the detector with respect to the axis of colliding beams [34].

The TileCal, positioned just 2.28 meters from the LHC beamline [35], experiences significant exposure to intense radiation due to its proximity. This harsh environment subjects its electronics, including PMTs, to substantial radiation damage. Over time, this exposure induces radiation fatigue, which progressively degrades the performance of these components.

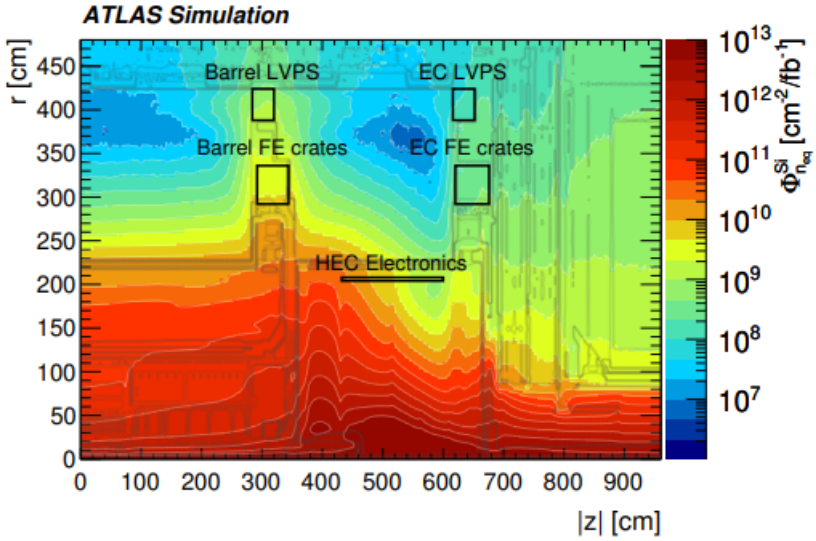


Figure 4.2: Radiation levels which the electronics found in the calorimeter systems in the ATLAS detector are subjected to [8]. Here FE crates are the "Front-End" crates which house readout electronics and LVPS refers to the "Low Voltage Power Supplies".

Region	|z| [cm]	r [cm]	TID [Gy/fb^{-1}]	$\Phi^{Si}_{n_{eq}}$ [cm^{-2}/fb^{-1}]	Φ^{had}_{20} [cm^{-2}/fb^{-1}]
Barrel FE crates	318	314	1.42×10^{-1}	3.80×10^{9}	6.50×10^{8}
HEC Electronics	516	206	8.00×10^{-2}	7.15×10^{9}	4.44×10^{8}
Barrel LVPS	302	406	1.97×10^{-2}	1.00×10^{9}	1.45×10^{8}
EC FE crates	648	314	1.88×10^{-2}	3.40×10^{8}	4.14×10^{7}
EC LVPS	634	406	5.9×10^{-3}	1.31×10^{8}	1.33×10^{7}

Figure 4.3: Total ionizing dose and characteristic particle fluences, obtained from GEANT4 simulations for the electronic systems shown in Figure 4.2 [8].

In figure 4.3 the distance along the beamline, denoted by $|z|$ (cm), indicates the absolute position of these electronics relative to the interaction point. The radial distance, r (cm), describes their location from the beamline in the transverse plane. The total ionizing dose (TID), measured in Gray per inverse femtobarn (Gy/fb^{-1}), quantifies the radiation dose absorbed by these electronics per unit of integrated luminosity. The 1 MeV neutron equivalent fluence, denoted as $\Phi^{\mathrm{Si}}_{\mathrm{n_{eq}}}$ (cm^{-2}/fb $^{-1}$), represents the exposure to neutral particles, normalized to integrated luminosity. Finally, the flux of hadrons,

denoted as Φ_{20}^{had} ($\text{cm}^{-2}/\text{fb}^{-1}$), indicates the exposure to hadronic particles with kinetic energy above 20 MeV, also normalized to integrated luminosity.

In order to study the radiation fatigue of the selected dynode materials, the samples were exposed to radiation doses akin to those found within the ATLAS detector, by exposing the materials to the decay products of an intense Co-60 source.

4.1 Decay of Cobalt-60

Cobalt-60 is an unstable nucleus which has a half-life of 5.27 years [36]. Co-60 is produced by the bombardment of the stable Co-59 isotope with neutrons in a nuclear reactor [37]. The nuclear reaction is given by:

$$^{59}_{27}\text{Co} + ^{1}_{0}\text{n} \longrightarrow ^{60}_{27}\text{Co} \tag{4.1}$$

In order for the nucleus to return to a stable state, the Cobalt-60 undergoes beta decay. Beta decay occurs when a nucleus is in an unstable state due to either the number of protons or neutrons. In beta-plus decay, if the nucleus has an excess of protons, a proton is converted into a neutron, emitting a positron and a neutrino in the process. In beta-minus decay, if the nucleus has an excess of neutrons, a neutron is converted into a proton, emitting an electron and an electron antineutrino in the process.

In the case of Co-60 there is an excess in the number of neutrons. To achieve stability, Co-60 undergoes beta-minus decay, as described by the nuclear reaction:

$$^{60}_{27}\text{Co} \longrightarrow ^{60}_{28}\text{Ni}^{*} + \text{e}^{-} + \bar{\nu}_e \tag{4.2}$$

Here:

- $^{60}_{27}$Co represents the Cobalt-60 nucleus which contains 27 protons and 33 neutrons.
- $^{60}_{28}\text{Ni}^{*}$ represents the excited state of the Nickel-60 nucleus.
- e^{-} is the electron (beta particle) emitted in the decay process.
- $\bar{\nu}_e$ is the electron antineutrino emitted.

In order for the Nickel nucleus to transition from the excited state ($^{60}_{28}\text{Ni}^{*}$) to the ground state ($^{60}_{28}$Ni), two possible decay mechanisms can occur:

- Two-Gamma Transition:

$$^{60}_{28}\text{Ni}^{*} \longrightarrow {}^{60}_{28}\text{Ni} + 2\,\gamma(1.17\ \text{MeV}\ \ \&\ \ 1.33\ \text{MeV}) \tag{4.3}$$

  This mechanism has a 99.88% likelihood. The process begins with the emission of a 1.1732 MeV gamma-ray, followed by the emission of a 1.3325 MeV gamma-ray. The energy of the electron emitted during the beta decay is approximately 0.31 MeV.

- Single-Gamma Transition:

$$^{60}_{28}\text{Ni}^{*} \longrightarrow {}^{60}_{28}\text{Ni} + \gamma(1.33\ \text{MeV}) \tag{4.4}$$

  This mechanism has a 0.12% likelihood. In this case, the excited nickel nucleus directly transitions to the ground state by emitting a single 1.3325 MeV gamma-ray. The energy of the electron emitted during the beta decay is approximately 1.48 MeV.

Explanation of probabilities:

Cobalt-60 ($^{60}_{27}$Co) has a spin-parity of $J^P = 5^+$. In the case of the two-gamma decay pathway the beta decay leads to an excited state of Nickel-60 ($^{60}_{28}$Ni*) which has a spin-parity of $J^P = 4^+$. This excited state decays by passing through an intermediate excited state of Nickel-60 ($^{60}_{28}$Ni*), which has a spin-parity of $J^P = 2^+$, and emits a 1.17 MeV gamma-ray. Subsequently the emission of a 1.33 MeV gamma-ray transitions the nucleus to its ground state ($^{60}_{28}$Ni) with a spin-parity of $J^P = 0^+$ [38].

On the other hand the decay pathway with a likelihood of 0.12% involves a direct transition from the spin-parity of $J^P = 4^+$ to the ground state ($J^P = 0^+$), bypassing the intermediate state. Due to the large change in spin-parity ($\Delta J = 4$), this direct transition is far less likely to occur compared to the two-gamma decay pathway.

The decay process of Co-60 to the ground state of Ni-60 can be represented as:

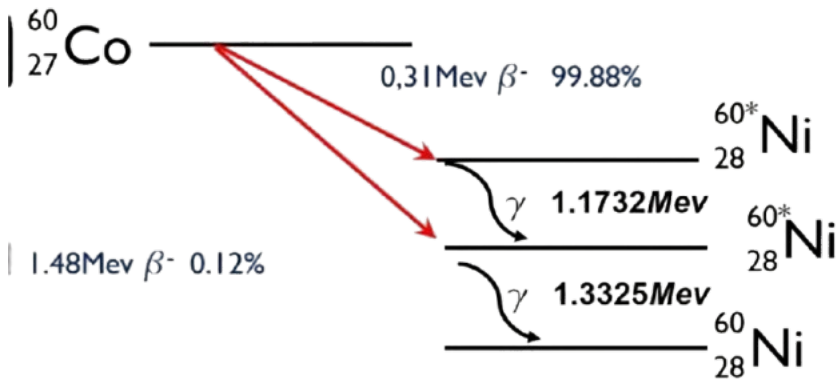


Figure 4.4: This figure illustrates the decay pathway of Cobalt-60 ($^{60}_{27}$Co) to the ground state of Nickel-60 ($^{60}_{28}$Ni). This image illustrates the two possible decay pathways (given by the two red lines) and the energies of the electrons emitted for both possible pathways as well as the energies of the gamma-rays emitted at each stage [39].

4.2 Cobalt-60 Facility

Samples of the materials used in this study were taken to the CERN Co-60 facility in Prévessin, France. At the Cobalt-60 facility, 9 samples of each material were exposed to three different radiation doses, with 3 samples per dose. The doses were set at 5 kGy, 50 kGy, and 100 kGy, aiming to study the effects of radiation at these varying dose levels on the electron yield of these materials.

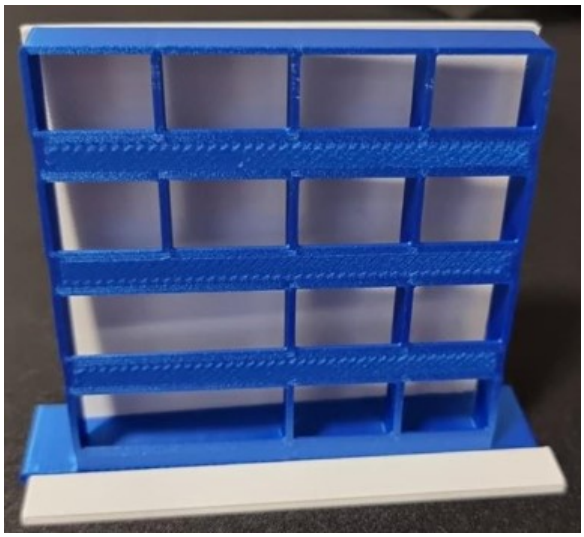


Figure 4.5: A 3D-printed sample holder was used to contain all the samples for this study. The holder was made from polylactic acid (PLA), and three such holders were printed to accommodate the samples at the three different dose levels.

The dose each group of samples would receive is found by calculating the dose delivered by the source at each of the locations of the sample holders (Figure 4.6) and determining the exposure time needed to reach the desired dose.

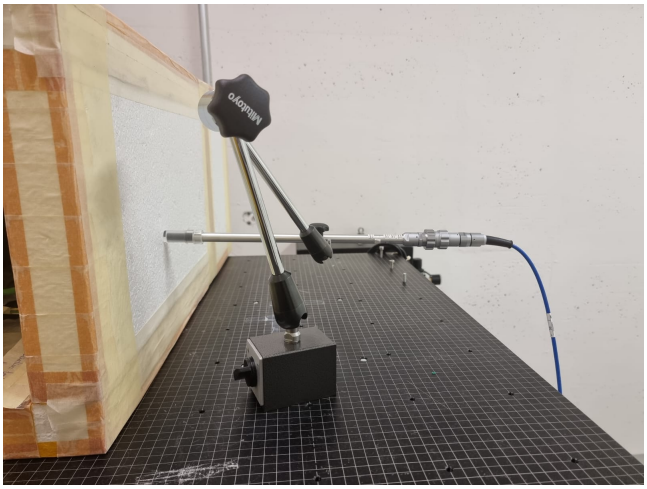


Figure 4.6: A calibrated cylindrical ionization chamber probe, Farmer-type, which measures radiation levels, is positioned at the location where the sample holder will be placed. This probe serves as the primary reference for quantifying the dose or activity arriving from the source at that specific distance. The probe is connected to a data acquisition system, as shown in Figure 4.8.

The data acquisition system shown in Figure 4.6 provides the radiation dose in mGy/s, enabling the calculation of the time dependency, specifically the duration for which the

samples need to be exposed to reach the desired dose.

Table 4.1: Irradiation conditions for different sample groups exposed to the Cobalt-60 source

Target Dose	**Distance from Source**	**Dose Rate (kGy/s)**	**Time at Position (days)**	**Dose at Position (kGy)**	**Total Dose (kGy)**
100 kGy	20.00 ± 0.05 cm	0.1164 ± 0.000005	10.828 ± 0.00001	–	108.975 ± 0.000005
50 kGy	80.00 ± 0.05 cm	0.01062 ± 0.000005	10.825 ± 0.00001	9.935 ± 0.000005	49.349 ± 0.000005
	20.00 ± 0.05 cm	0.1164 ± 0.000005	3.919 ± 0.00001	39.414 ± 0.000005	
5 kGy	88.00 ± 0.05 cm	0.008773 ± 0.000005	6.846 ± 0.00001	–	5.192 ± 0.000005



Figure 4.7: Window of the Cobalt-60 source (approximately 20 cm away from the source), along with the samples designated to receive 100 kGy, housed in one of the sample holders.



Figure 4.8: The dose reading was taken by a probe located approximately 88 cm away from the Cobalt-60 source. This is the region where the samples designated to receive 5 kGy were housed in the sample holder.

4.2.1 SEY Experimental Background

iThemba LABS is South Africa's largest national research facility dedicated to multi-disciplinary scientific studies. It operates the most extensive accelerator infrastructure in the southern hemisphere [40]. Among its key divisions, the Tandem and Accelerator Mass Spectrometry (TAMS) facility in Johannesburg houses a 6 MV Tandem accelerator that supports several specialized beamlines, including those for Accelerator Mass Spectrometry (AMS), Nuclear Physics, Heavy Ion - Elastic Recoil Detection Analysis (HI-ERDA), and the Nuclear Microprobe. The Nuclear Microprobe beamline facilitates analytical techniques such as Rutherford Backscattering Spectroscopy (RBS), Ion Beam Analysis (IBA), and Micro-Particle Induced X-ray Emission (Micro-PIXE) [41].

For this study, the microprobe beamline was adapted—through the addition of two external instruments — to enable the measurement of the secondary electron yield (SEY) of Al_2O_3 and MgO samples. These modifications facilitated EEY measurements under conditions akin to its standard environmental conditions.

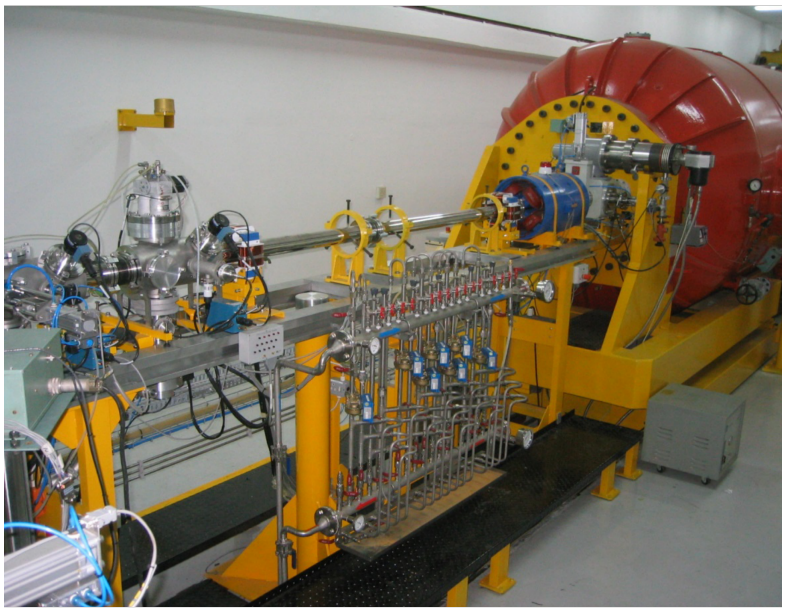


Figure 4.9: 6 MV Tandem Accelerator located at the iThemba LABS, Johannesburg.

4.3 Experimental Procedure

A 2 MeV proton beam was generated by the 6 MV Tandem accelerator at the TAMS facility and directed towards the nuclear microprobe beamline. A Faraday cup was used to collect and measure the current of the proton beam. The current was adjusted to 70 nA, and the beam was focused to an area of 500 $\times$ 500 μm^2. The beam was also set to scanning mode, with the scanning area set to 500 $\times$ 500 μm^2 over the sample's surface. The scanning mode was employed to get a more general measurement of the sample surface as opposed to one spot in order to reduce extensive damage to the sample.

A detachable carousel is integrated into the microprobe chamber setup. The chamber is vacuum-sealed and pumped to achieve a pressure of $10^{-}6$ Pa in order to reduce gas ionization which would influence the SEY measurements. The carousel is electrically insulated from the microprobe chamber and is connected to external equipment via a feed-through channel.

Each Al_2O_3 and MgO sample was first mounted onto a metallic disc using graphite-based conductive paste for electrical contact, then clipped into the microprobe carousel (Figure 4.10). The samples were enclosed within a dome-shaped brass cage (this cage has an insulating Teflon base so that no electrical contact is made between the cage and the carousel to avoid leakage current), which featured a centrally positioned Teflon

piece with an aperture (approximately 5mm in diameter) to allow the proton beam to pass through and interact with the sample without interference from the brass to avoid excess electronic noise. To ensure stability during the experiment, the brass cage was secured to the carousel using a temporary adhesive rubber.

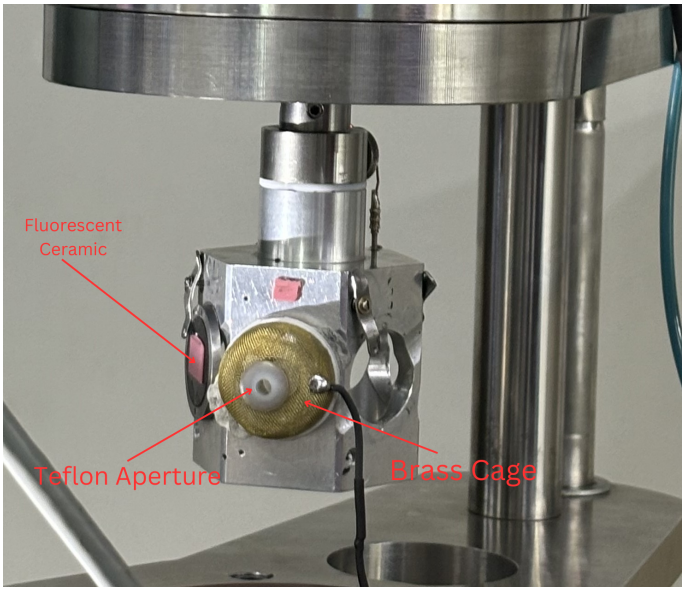


Figure 4.10: Microprobe Carousel Setup: Showing the Teflon aperture, brass cage, and a fluorescent ceramic.

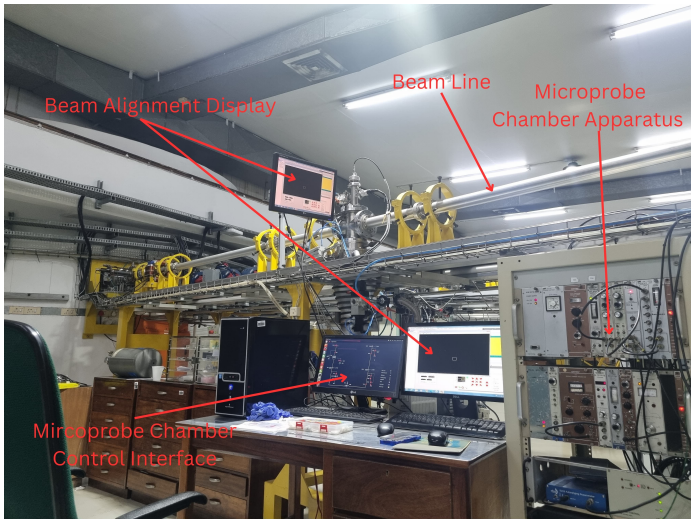


Figure 4.11: The microprobe chamber control interface is used for all microprobe chamber-related processes, such as vacuum pumping, venting, and other operational controls.

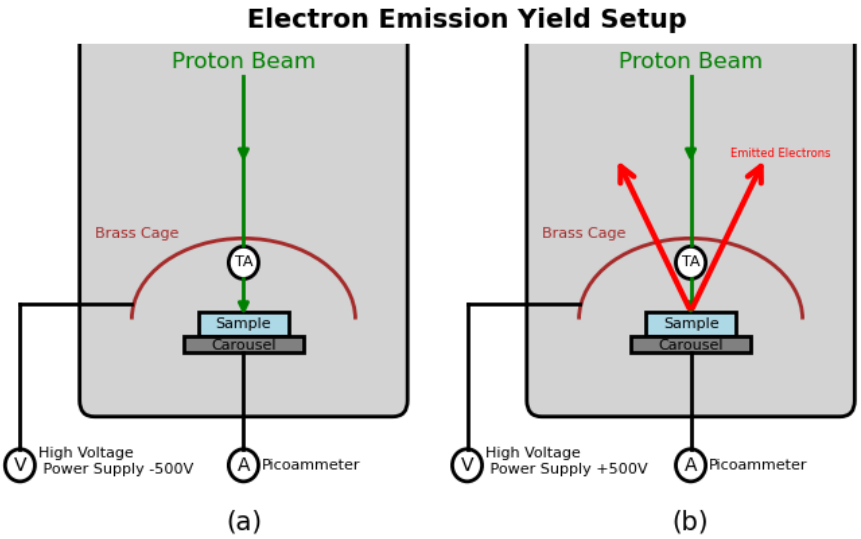


Figure 4.12: Experimental setup used to determine the EEY of the MgO and Al_2O_3 samples.

Figure 4.12 illustrates the experimental setup used in this study to measure the electron emission yield of the MgO and Al_2O_3 samples. In both configurations, the proton beam passes through the Teflon aperture, labeled TA in the figure. Subfigure (a) shows the setup when a negative voltage bias of -500 V is applied to the brass cage, with the high-voltage power supply connected via a feed-through cable. In this configuration, the electrons emitted from the target are suppressed, as the negative bias applied to the brass cage repels them back toward the sample surface, and the measured current primarily represents the beam current. The picoammeter records this current, connected to the microprobe carousel through a BNC feed-through.

Subfigure (b) depicts the configuration when the high-voltage power supply is set to +500 V and connected to the brass cage. Here, the positive voltage bias facilitates electron emission by attracting emitted electrons from the sample surface, which are then measured. This setup allows for the measurement of electron emission yield, as the difference between the current measured under positive and negative bias reflects the yield of emitted electrons. This approach follows the principles described in [42].

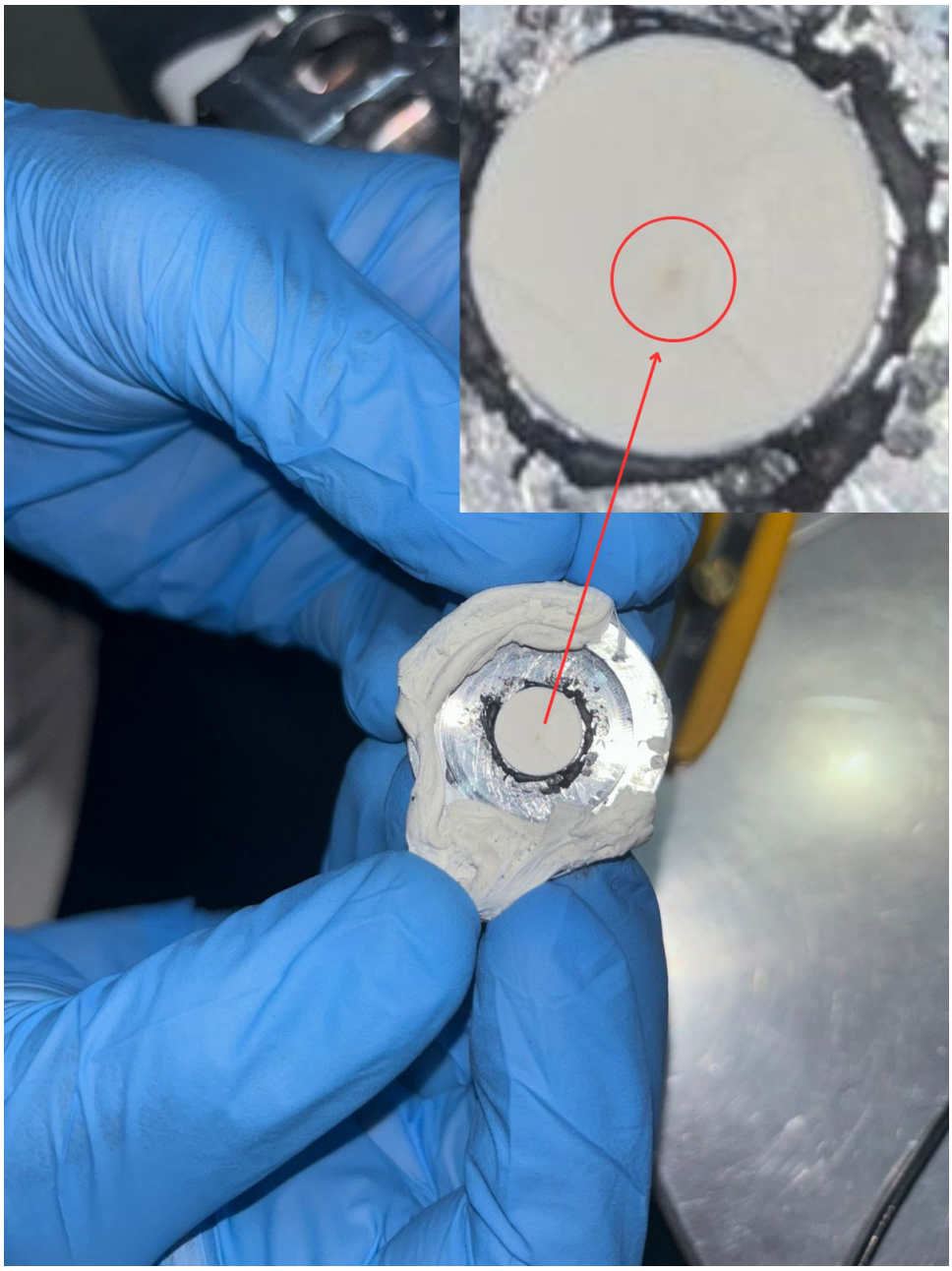


Figure 4.13: Al_2O_3 sample mounted on a metallic disc using graphite-based conductive paste, with a temporary rubber adhesive securing the brass cage over the sample.

Graphite-based conductive paste is applied to ensure proper electrical contact between the sample and the disc. Adhesive rubber is placed around the fringe to secure the brass cage and ensuring electrical isolation from the sample carousel. Upon closer inspection, a faint darkened region can be seen on the sample's surface (this mark was only visible on the Al_2O_3 samples), marking the spot where the proton beam was incident during irradiation. This beam mark indicates the interaction area where the electron emission

yield was generated.

The microprobe chamber, which was evacuated to a pressure of 10^{-6} Pa. An ORTEC 456 power supply is connected via feed-through to the brass cage and is used to apply voltage biases of +500V and -500V to the brass cage, while the Keithley 6485 is also connected via feed-through to the carousel to measure the current.

Before data collection, the alignment of the proton beam was verified using a section of the carousel fitted with fluorescent ceramic. When the beam strikes the ceramic, it illuminates and becomes visible on the alignment monitor (see Figure 4.11). Since the ceramic is positioned on the same plane as the carousel, its illumination confirms that the beam will strike the mounted sample on the carousel. To align the beam with the sample, the carousel, which is comprised of 8 faces marked by angles, must be rotated. The sample's position is also marked by an angle, so once the ceramic is illuminated, the carousel must be manually rotated back to the marked angle (using external system controls) to ensure the beam is incident on the sample.

Current measurement procedure:

1. The picoammeter is set to stabilize for 30 seconds with no proton beam exposure. Using this period post measurement, the average current is calculated and used as the offset, which is then subtracted from all subsequent data points.

2. The Faraday cup serves as a beam shutter for this measurement. Once it is removed, the proton beam interacts with the sample. Data acquisition begins with the high-voltage power supply set to +500 V, and current measurements are recorded for 120 seconds. LabVIEW serves as the interface for data acquisition from the picoammeter, recording the current at a rate of one measurement per second.

3. After the 120-second data acquisition period, the Faraday cup is reinserted to block the proton beam, marking the end of the measurement. This results in a total of 150 seconds of data collection: 30 seconds for offset determination and 120 seconds for the actual measurement.

4. The polarity of the high-voltage power supply is reversed to -500 V, and the same procedure is repeated for the negative voltage measurement.

5. Each measurement was repeated three times per sample. However, due to localized damage induced by the proton beam, the later measurements were affected. As a result, only the first complete measurement is presented in this thesis.

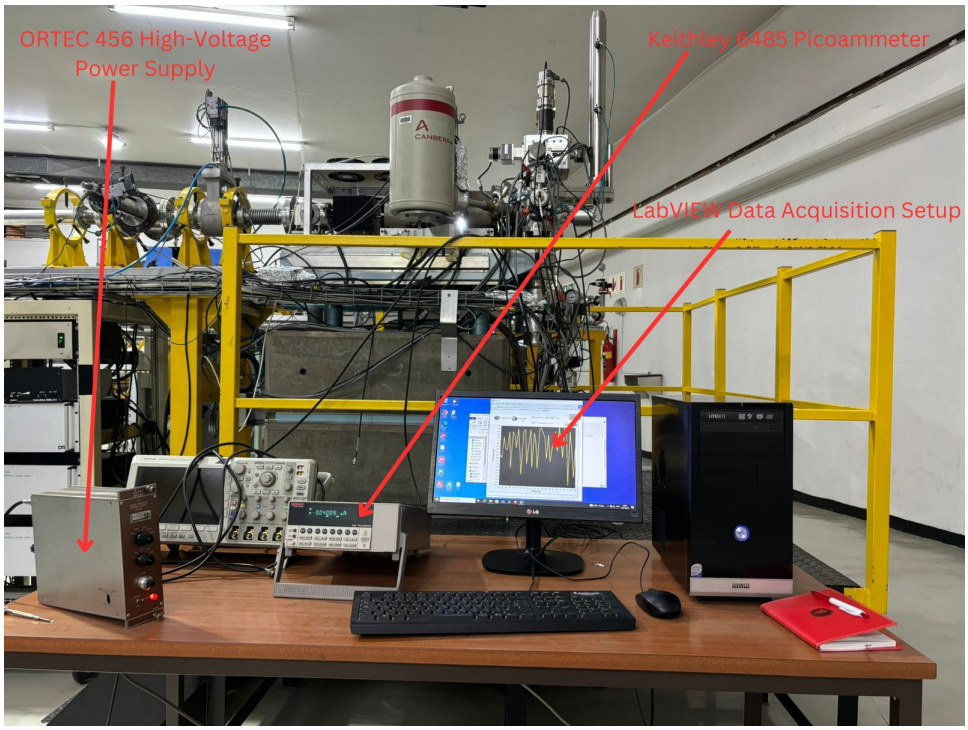


Figure 4.14: Data Acquisition Setup.

This setup essentially performed two measurements for each sample—one under positive voltage and another under negative voltage. A voltage bias of ± 500V is preferential to lower voltages to intensify the desired effects.

The necessity of the two measurements is due to the fact that EEY of the Al_2O_3 and MgO samples can be calculated using the following formula [42]:

$$\delta = \frac{\sum I^+}{\sum I^-} - 1 \tag{4.5}$$

Where I^+ represents the current measurement under positive 500V bias and I^- represents the current measurement under negative 500V bias.

Or simply:

$$\delta = \frac{\sum I^+ - \sum I^-}{\sum I^-} \tag{4.6}$$

Here I^+ and I^- are a single averaged data point, averaged over 120 seconds of data acquisition. For the purposes of this study, the electron emission yield will be determined using the average current values rather than the summation of terms in the equation.

Thus, the final equation to be used is:

$$\delta = \frac{\overline{I^+} - \overline{I^-}}{\overline{I^-}} \tag{4.7}$$

Chapter 5

Results and Discussion

5.1 Radiation Damage and Absorbed Dose Simulations

5.1.1 FLUKA

To comprehensively evaluate the effects of radiation-induced damage and the absorbed gamma radiation dose on the sample at various exposure levels, the FLUKA simulation software was employed to model the radiation environment and its impact. FLUKA is a fully integrated Monte Carlo particle physics simulation package that offers extensive capabilities in areas such as high-energy experimental physics, radiation shielding, detector design, dosimetry, medical physics, and radiobiology [43, 44].

FLUKA is capable of handling various components of radiation from thermal energies (for neutrons) and energies from 1 keV up to cosmic ray energies and has been benchmarked against numerous experimental datasets in order to verify the validity [45]. For this study, FLAIR, a user-friendly graphical interface for FLUKA, was utilized to streamline the preparation of input files and the execution of simulations, enhancing the overall efficiency of the workflow [46].

5.1.2 Simulations

The two photonic process used by FLUKA to simulate radiation damage induced by photons are pair production and Bremsstrahlung. In the Bremsstrahlung process the recoil is sampled randomly from an approximation of the momentum cross-section [47]:

$$\frac{d\sigma}{dp_\perp} = \frac{32\alpha(Z\alpha)^2}{kp_\perp^3}\left[1 - \frac{k}{E} + \frac{1}{2}\left(\frac{k}{E}\right)^2\right] ln\left(\frac{p_\perp}{m_e}\right) \tag{5.1}$$

- $\frac{d\sigma}{dp_\perp}$ is the differential cross section of the Bremsstrahlung process, with respect to the perpendicular momentum $p_\perp$.
- α is the fine structure constant
- Z is the atomic number of the target nucleus
- k is the energy of the Bremsstrahlung photon
- E is the energy of the incident electron
- m_e is the mass of the electron

For the pair production process FLUKA uses the following approximation to simulate the process [47]:

$$\frac{d\sigma}{dp} = \frac{0.183 \cdot 10^{-2} Z^2}{p^3} \left(ln\left(p\right) + 0.5\right) \tag{5.2}$$

Both Equation 5.1 and Equation 5.2 can approximated in the following way, thus FLUKA uses the following approximation for both processes:

$$\frac{d\sigma}{dp} \propto \frac{ln(p/c)}{p^3} \tag{5.3}$$

Where c is the minimum recoil momentum, equation 5.3 cannot be solved analytically, FLUKA thus uses a rejection sampling method that generates random samples from a probability distribution given by an equation that is similar to Equation 5.3 to calculate a metric called the displacement per atom (DPA) [45].

DPA measures the average number of times an atom in a material is displaced from its lattice position due to a given amount of radiation. For example, a DPA value of three indicates that, on average, each atom in the material has been displaced three times [45]. In this study, FLUKA's versatile capabilities were leveraged to calculate DPA, enabling a comprehensive evaluation of the radiation-induced damage sustained by the materials.

Absorbed dose quantifies the energy deposited in matter by ionizing radiation per unit mass. In this study, FLUKA was employed to simulate the absorbed dose in the two materials of interest across three varying radiation exposure levels. These simulations provided critical insights into the extent of radiation absorbed by the materials.

5.1.3 Geometries and Setup

For these simulations, the input files varied only in their scoring parameters, ensuring that the setups for the two simulations were nearly identical. Initially, the simulations focused exclusively on the number of photons interacting with the materials, excluding the emission of beta particles and electron antineutrinos from the Co-60 source. This simplified approach established a foundational baseline for analyzing Co-60 decay interactions with the materials.

To further refine this baseline, an average photon energy of 1.25285 MeV was employed. This value represents the average energy of photons emitted during the more probable decay path of Co-60, which involves the emission of two photons with energies of 1.1732

MeV and 1.3325 MeV. The purpose of these initial simulations was to establish a benchmark against which the results of subsequent, more comprehensive simulations could be compared.

The photons were modeled as a beam, and the total number of photons interacting with the target was calculated as follows:

- The Co-60 source had an activity of 70 TBq, in the decay path of Co-60 which involves two photon decay, there will be $1.4 \cdot 10^{14}$ photons emitted from the source per second over a solid angle of $4\pi sr$ (the solid angle of a sphere) with an averaged energy of 1.25285 MeV.
- The solid angle which the samples were at relative to the source was a function of their distance from the source, for completeness the solid angle and total number of photons received by the 100 kGy sample will be calculated:

$$\Omega = A/d^2 \tag{5.4}$$

Where Ω is the solid angle of the 100 kGy samples relative to the source, A is the area of the sample and d is the distance of the sample relative to the source.

$$\Omega = \frac{\pi \cdot (0.005\ m)^2}{(0.2\ m)^2} \tag{5.5}$$

$$\Omega = 0.0019635\ sr \tag{5.6}$$

In order to find the total number of photons which interacted with the 100 kGy samples, the solid angle is multiplied by the number of photons emitted from the source:

$$0.0019635\ sr \cdot \frac{1.4 \cdot 10^{14}}{4\pi} = 2.19 \cdot 10^{10}\ photons/s \tag{5.7}$$

The same calculation was done for the 5kGy and 50kGy samples which leads to the total number of photons per dose:

- 5 kGy: $1.55 \cdot 10^9$ photons/s
- 50 kGy: $2.43 \cdot 10^9$ photons/s at 80cm and $2.19 \cdot 10^{10}$ photons/s at 20cm (source window)
- 100 kGy: $2.19 \cdot 10^{10}$ photons/s

Once the number of photons required for each dose was known, the simulated results are as follows:

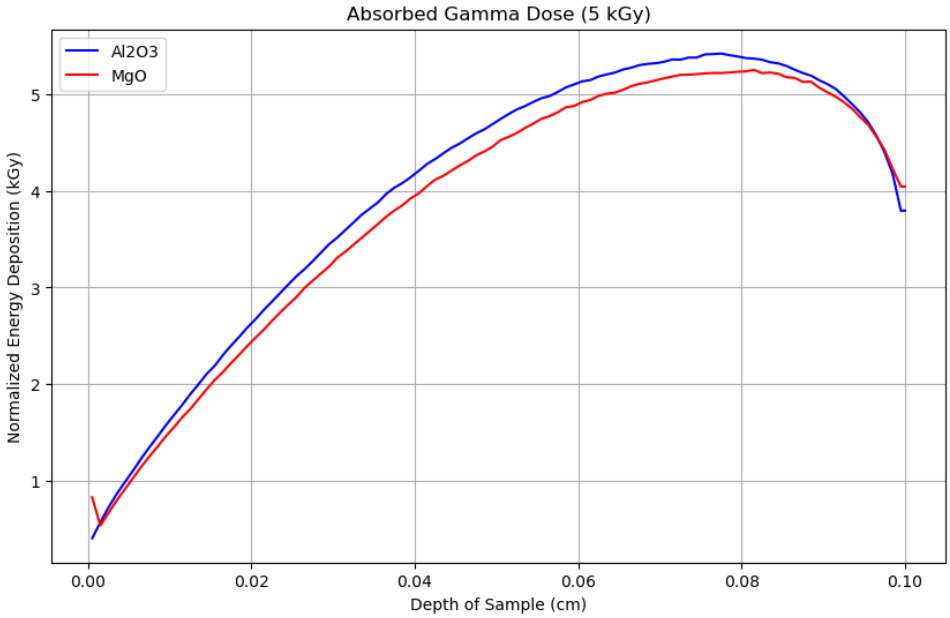


Figure 5.1: Simulated absorbed dose from a mono-energetic photon source (1.25 MeV) placed 88.00 cm ± 0.05cm away from the target for 6.846 ± 0.00001 days for the two samples.

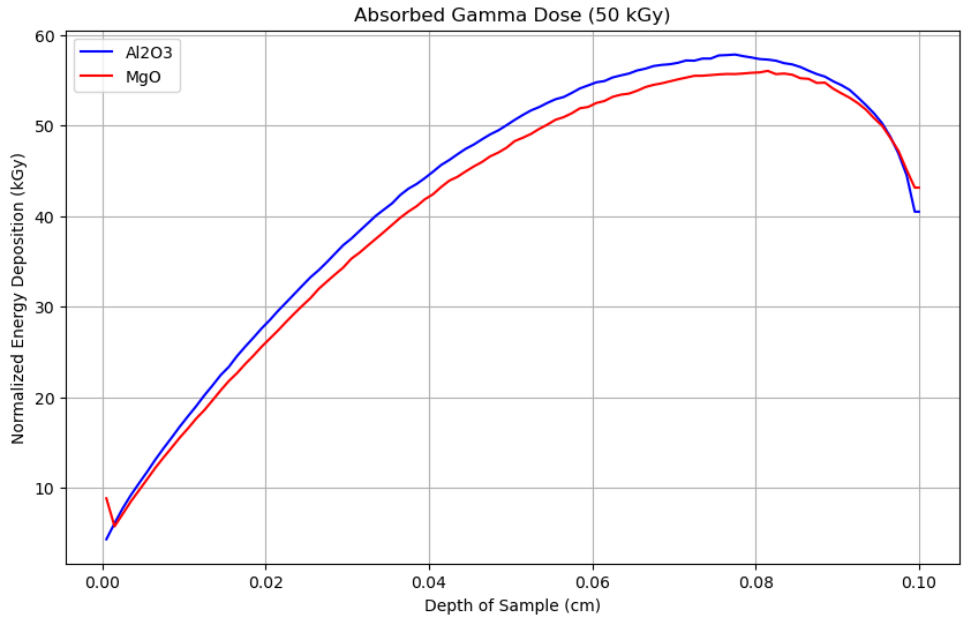


Figure 5.2: Simulated absorbed dose from a mono-energetic photon source (1.25 MeV) placed at a distance of 80.00 cm ± 0.05 cm from the target for 10.825 ± 0.00001 days and then placed at 20.00 ± 0.05cm from the target for 3.919 ± 0.00001 days for the two samples.

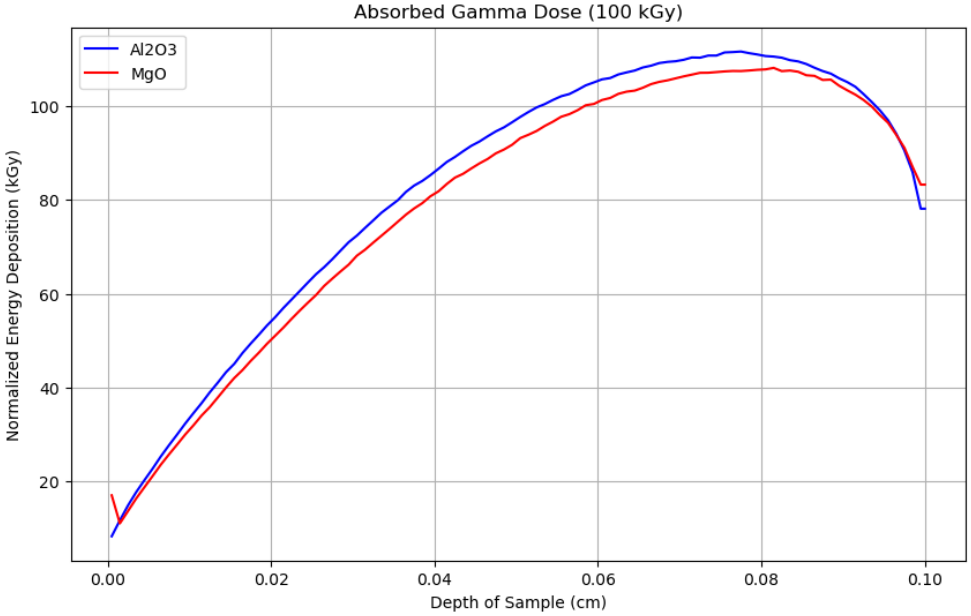


Figure 5.3: Simulated absorbed dose from a mono-energetic photon source (1.25 MeV) placed at a distance of 20.00 cm ± 0.05 cm from the target for 10.828 ± 0.00001 days for the two samples.

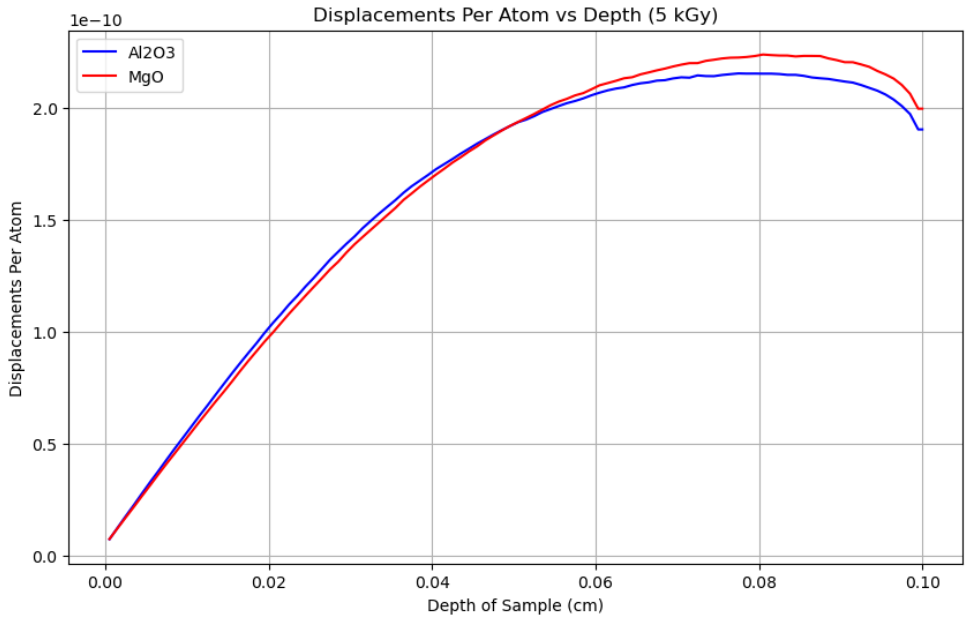


Figure 5.4: Simulated DPA from a mono-energetic photon source (1.25 MeV) placed 88.00 cm ± 0.05cm away from the target for 6.846 ± 0.00001 days for the two samples. Please note the scaling factor shown in the top left corner of the plot, and keep this in mind throughout the remainder of this thesis.

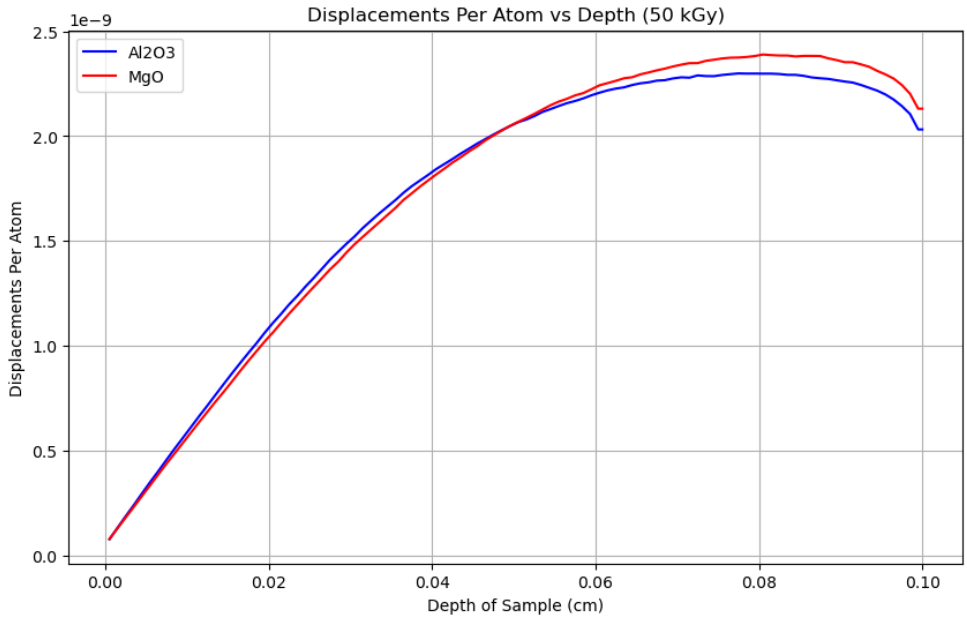


Figure 5.5: Simulated DPA from a mono-energetic photon source (1.25 MeV) placed at a distance of 80.00 cm ± 0.05 cm from the target for 10.825 ± 0.00001 days and then placed at 20.00 ± 0.05cm from the target for 3.919 ± 0.00001 days for the two samples.

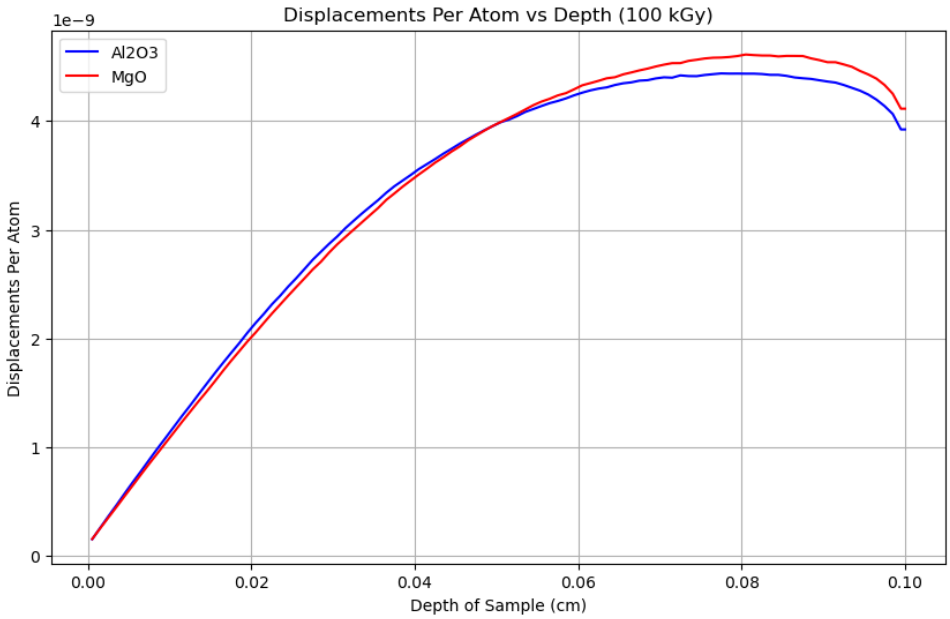


Figure 5.6: Simulated DPA from a mono-energetic photon source (1.25 MeV) placed at a distance of 20.00 cm ± 0.05 cm from the target for 10.828 ± 0.00001 days for the two samples.

The absorbed dose from the benchmark simulations aligns with the expected total dose that the samples were intended to receive. The dose reaches its maximum approximately three-quarters into the material. The displacement per atom (DPA) results from these simulations indicate that DPA increases with absorbed dose, with its maximum occurring near the region of highest energy deposition, which is consistent with expectations, since higher energy deposited generally leads to higher atomic displacements.

Upon completing the benchmark simulations, the final simulation input card was generated. The only modification in the final simulations was the replacement of the monoenergetic photon source with the actual photon energy spectrum of a Co-60 source, while maintaining the same activity (70 TBq) as the source used in the experimental facility. The absorbed dose in the final simulation includes contributions from pair production and bremsstrahlung, which are inherently accounted for by FLUKA's electromagnetic physics models based on the incident photon energies.

A comparison of the absorbed dose profiles from the benchmark and final simulations confirms strong agreement, validating the use of the Co-60 spectrum in place of the averaged energy used in the benchmark. Both simulations yield dose distributions consistent with the expected total exposure of 100 kGy.

The simulation geometry matched the physical sample dimensions, with a cylindrical

sample of 1 cm radius and 1 mm thickness. The distance between the Co-60 source and the target, as well as the total exposure time, were varied as described above depending on the intended dose, and were implemented directly into the simulation to replicate the experimental irradiation conditions.

5.1.4 Simulation Results

Absorbed Dose Simulations

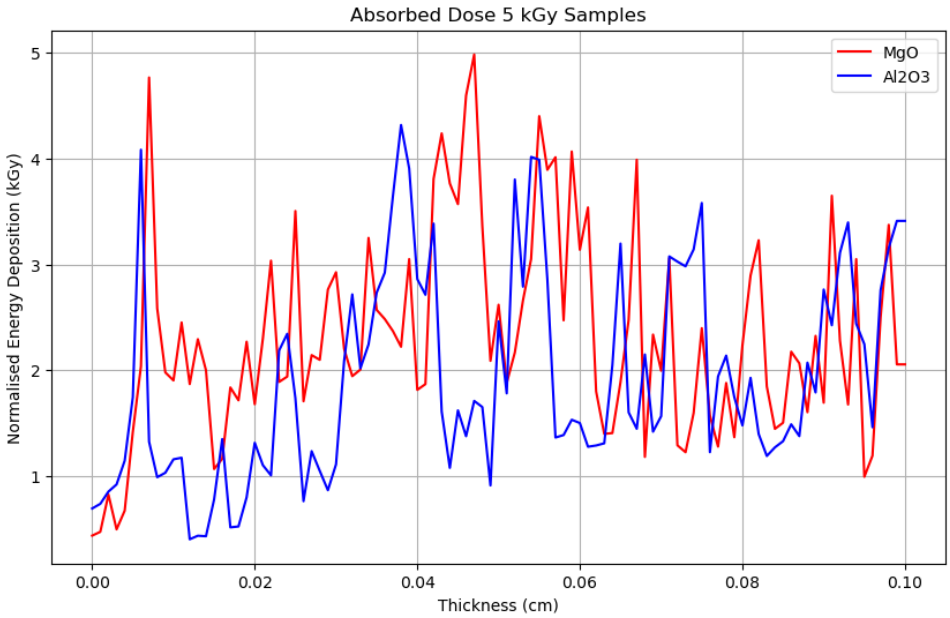


Figure 5.7: Simulated absorbed dose from a 70 TBq Co-60 source placed 88.00 cm ± 0.05cm away from the target for 6.846 ± 0.00001 days for the two samples.

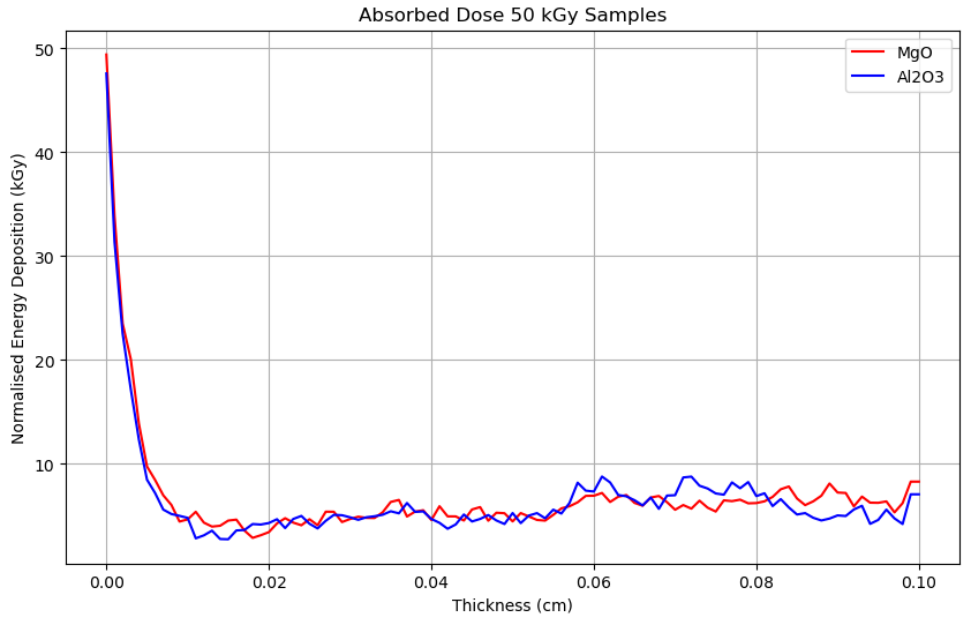


Figure 5.8: Simulated absorbed dose from a 70 TBq Co-60 source placed at a distance of 80.00 cm ± 0.05 cm from the target for 10.825 ± 0.00001 days and then placed at 20.00 ± 0.05cm from the target for 3.919 ± 0.00001 days for the two samples.

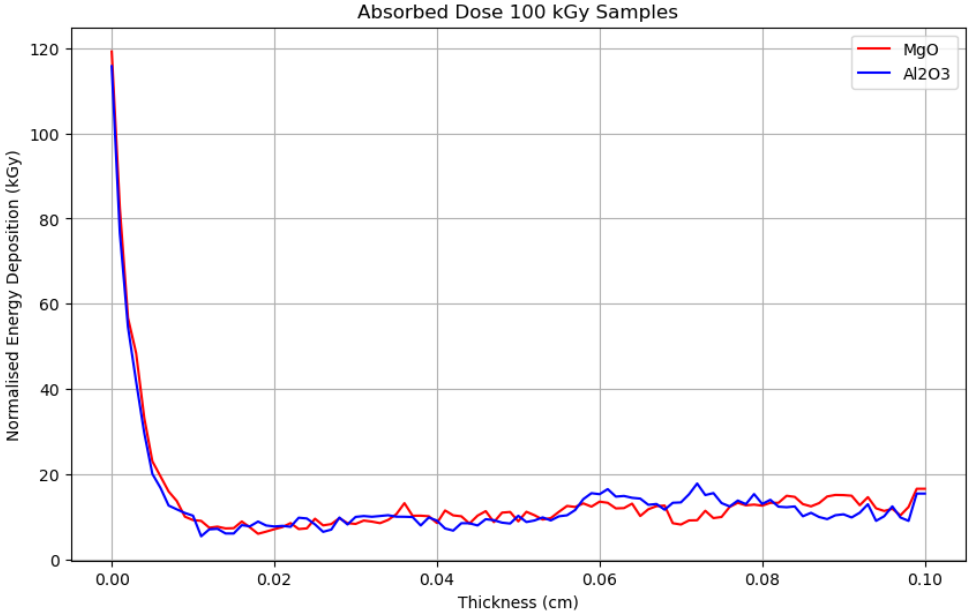


Figure 5.9: Simulated absorbed dose from a 70 TBq Co-60 source placed at a distance of 20.00 cm ± 0.05 cm from the target for 10.828 ± 0.00001 days for the two samples.

DPA

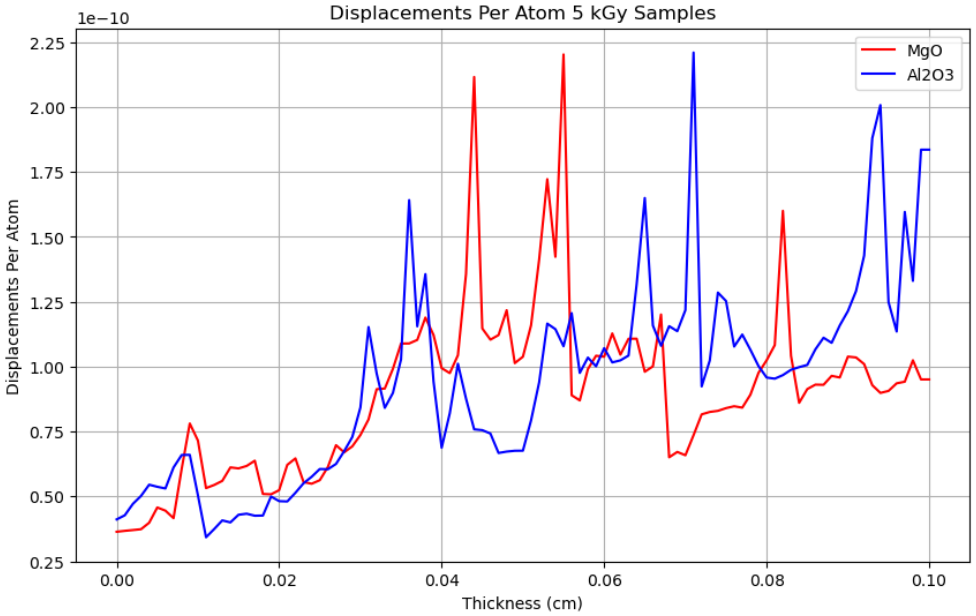


Figure 5.10: Simulated DPA from a 70 TBq Co-60 source placed 88.00 cm ± 0.05cm away from the source for 6.846 ± 0.00001 days for the two samples.

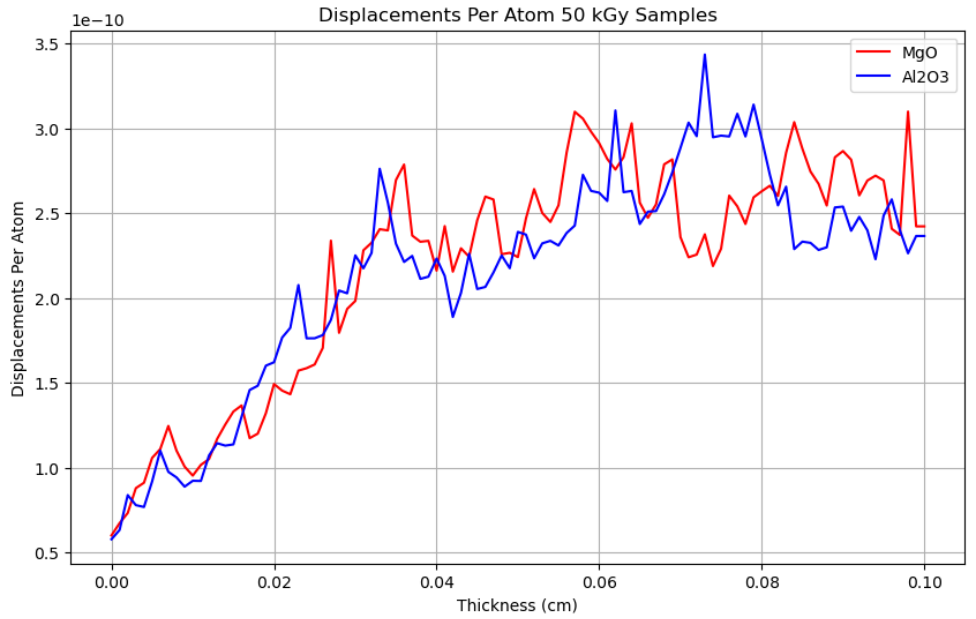


Figure 5.11: Simulated DPA from a 70 TBq Co-60 source placed at a distance of 80.00 cm ± 0.05 cm from the source for 10.825 ± 0.00001 days and then placed at 20.00 ± 0.05cm from the source for 3.919 ± 0.00001 days for the two samples.

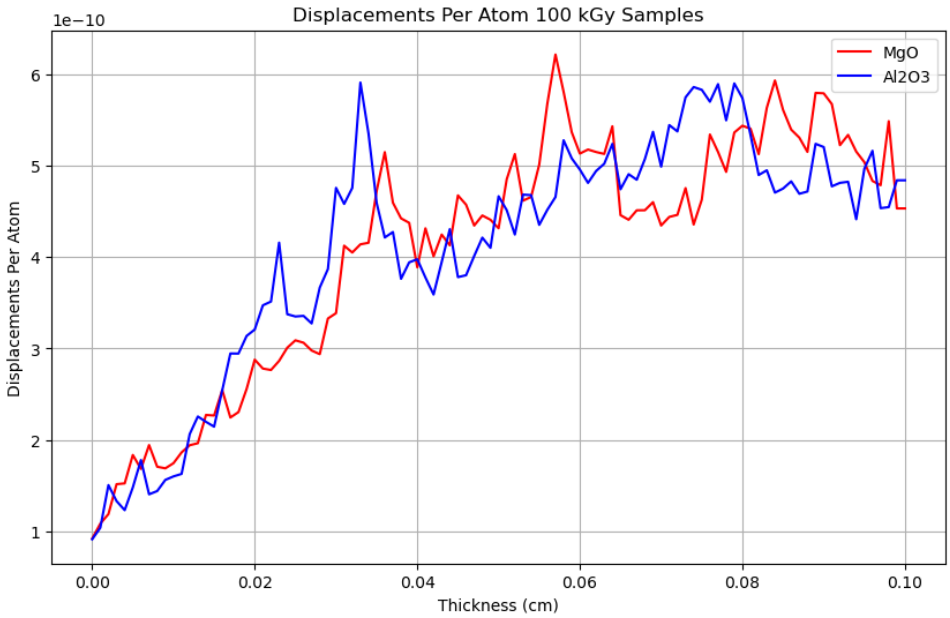


Figure 5.12: Simulated DPA from a 70 TBq Co-60 source placed at a distance of 20.00 cm ± 0.05 cm for 10.828 ± 0.00001 days for the two samples.

Upon reviewing the completed simulations, a clear difference in absorbed dose distribution between the benchmark and final simulations can be observed. In the final 5 kGy absorbed dose simulations, the energy deposition remains relatively consistent throughout the material. This contrasts with the benchmark simulations, where the absorbed dose increased almost linearly before reaching a maximum at approximately three-quarters into the material.

With regard to the final simulations of the 50 kGy and 100 kGy absorbed dose cases, a stark contrast is observed compared to both the benchmark simulations at the same absorbed doses and the final 5 kGy absorbed dose simulation. In the 50 kGy and 100 kGy final simulations, the absorbed dose is at its maximum near the surface of the material and then drops off significantly deeper below the surface of the material.. This indicates that, unlike the benchmark simulations, where the absorbed dose followed a more gradual increase before peaking deeper into the material, the majority of the energy deposition in these higher-dose cases occurs at the surface, with far less energy penetrating deeper into the material.

The observed results can be explained by the electrons emitted from the Co-60 source. Using the ESTAR tool [48], developed by the NIST, we simulate the stopping range of an electron in air. ESTAR provides the CSDA (Continuous Slowing Down Approximation) range in units of (g/cm^2). The kinetic energy used in the simulation is 0.3 MeV, which is close to the 0.31 MeV energy of the electrons emitted from Co-60 decay. To

determine the stopping range of an electron in air, we divide the CSDA by the density of air.

$$Stopping\ Range\ = \frac{CSDA\ Range\ (g/cm^2)}{Density\ of\ air\ (g/cm^3)} \tag{5.8}$$

$$Stopping\ Range\ = \frac{9.528 \cdot 10^{-2}\ (g/cm^2)}{0.001293\ (g/cm^3)} \tag{5.9}$$

$$Stopping\ Range\ \approx 73.7\ cm \tag{5.10}$$

This implies that both the 100 kGy and 50 kGy samples were irradiated by both electrons and photons from the Co-60 source.

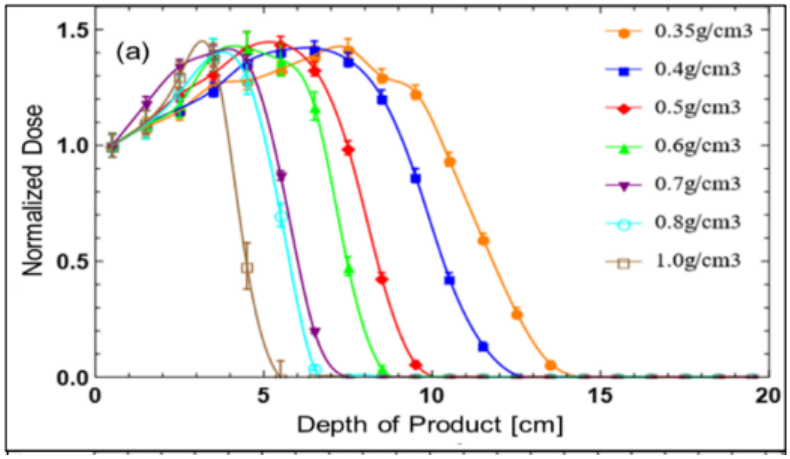


Figure 5.13: This figure serves as a reference for the normalized dose (Gy) distribution of a 10 MeV electron beam, exhibiting characteristics similar to those observed in the final simulations presented above [49]. Although the material densities used in the referenced figure are higher than those employed in this study, the figure is included to demonstrate the simulation's ability to reproduce experimental trends.

In terms of DPA, both the benchmark and final simulations yielded values on the same order of magnitude. The discrepancy between the DPA of the benchmark simulation and the final simulation is primarily attributed to the depth at which energy is deposited within the sample. In the benchmark simulations, the absorbed dose increased with the material's thickness, leading to a corresponding increase in the DPA. In contrast, the energy deposition in the final simulations was more complex.

For the 5 kGy sample, the energy deposition was nearly uniform, peaking in the centre of the sample. The DPA for this dose increases steadily until it reaches approximately

halfway through the sample, after which it gradually decreases. In the case of the 50 kGy and 100 kGy samples, the DPA increases sharply from the surface of the material to about halfway through the sample, where it then levels off. This sharp increase in DPA near the surface can be attributed to the electronic damage occurring at shallow depths within the material.

5.2 Offset Correction

As mentioned in Chapter 4 each measurement of the Keithley 6485 Picoammeter was given 30 second during which to stabilize. The purpose of this stabilization period is to reduce systematic errors as well as baseline shifts in the measurements. This offset correction ensures that the measurements being compared (positive and negative bias) are as accurate as possible. The offset/stabilization period can be seen in the following figure:

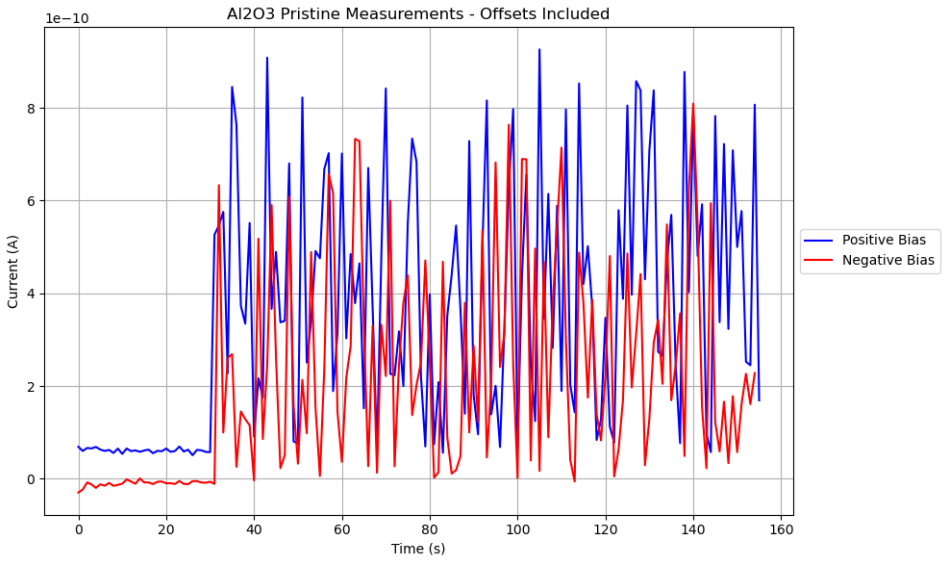


Figure 5.14: Current Vs Time measurements for the Al_2O_3 Pristine sample, including both the negative and positive bias and their respective offset measurements included.

As illustrated in the figure above, the initial stabilization period of the picoammeter resulted in current values that were not equal to zero. This non-zero offset during the settling phase necessitates a correction. To address this, the average current during the stabilization period was calculated and subtracted from the beam current measured during the 120s when the bias voltage was applied to the brass cage. If the offset was positive and added if the offset was negative. This offset correction was applied consistently across all calculations and figures presented throughout the remainder of this chapter.

5.3 Current Measurements as a Function of Dose

In this subsection, the offset-corrected current measurements obtained during the 120-second data collection periods are presented for all Al_2O_3 and MgO samples. These measurements were recorded at a rate of one data point per second, resulting in a total of 120 data points per measurement period. Each current value has been corrected by applying the corresponding offset, which was determined during the initial 30-second stabilization period prior to data acquisition.

The figures presented below illustrate the current measurements described in Figure 4.12. A consistent trend is observed, where the measured current during the positive bias runs is significantly higher than that observed during the negative bias runs. This behavior is rooted in the interaction between the applied bias voltage and the behavior of secondary electrons emitted from the sample surface.

When a positive bias is applied to the surrounding brass cage, it creates an electric field that attracts secondary electrons emitted from the sample toward the cage. These electrons are no longer collected by the sample (which is connected to the picoammeter), resulting in a net loss of negative charge from the sample. Consequently, this leads to a higher positive current being registered by the picoammeter.

In contrast, when a negative bias is applied to the brass cage, the electric field repels the emitted secondary electrons back toward the sample. This suppression of electron escape causes more electrons to return to the sample surface, thereby reducing the net current leaving the sample. As a result, the current measured by the picoammeter is lower in magnitude, since fewer electrons are lost to the surrounding environment.

This observed asymmetry in current under different bias polarities is a direct manifestation of secondary electron emission dynamics and is crucial for evaluating the secondary electron yield (SEY) characteristics of the irradiated materials.

5.3.1 Magnesium Oxide

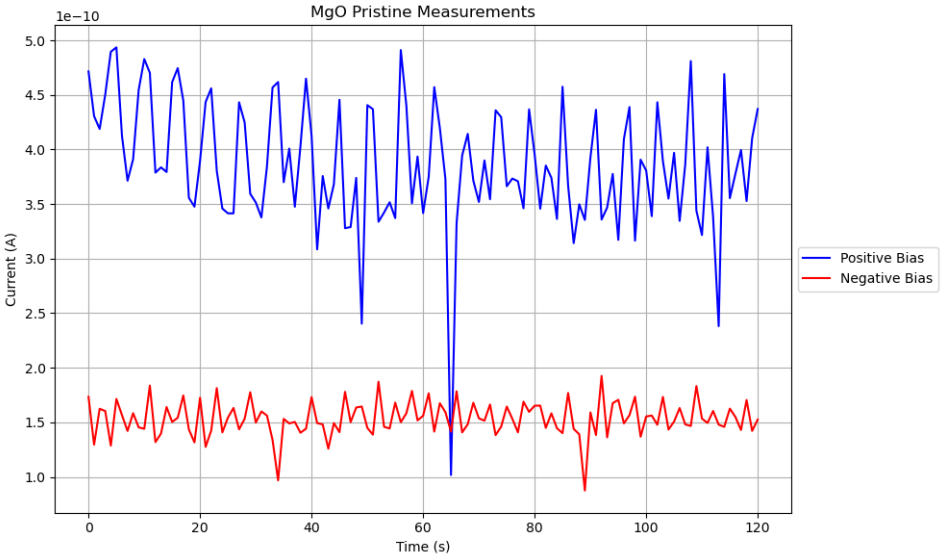


Figure 5.15: Measured current under positive and negative applied voltage bias for pristine Magnesium Oxide.

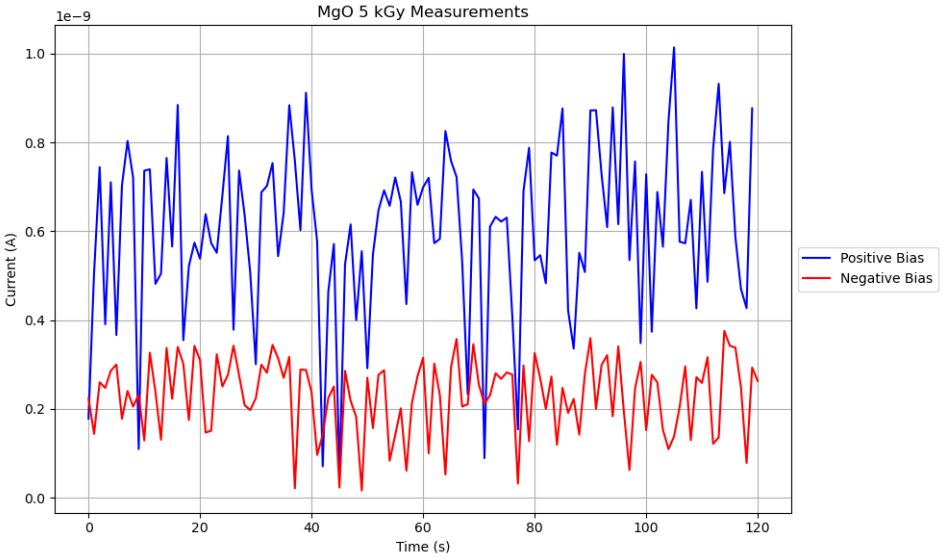


Figure 5.16: Measured current under positive and negative applied voltage bias for Magnesium Oxide samples with an absorbed gamma radiation dose of 5 kGy.

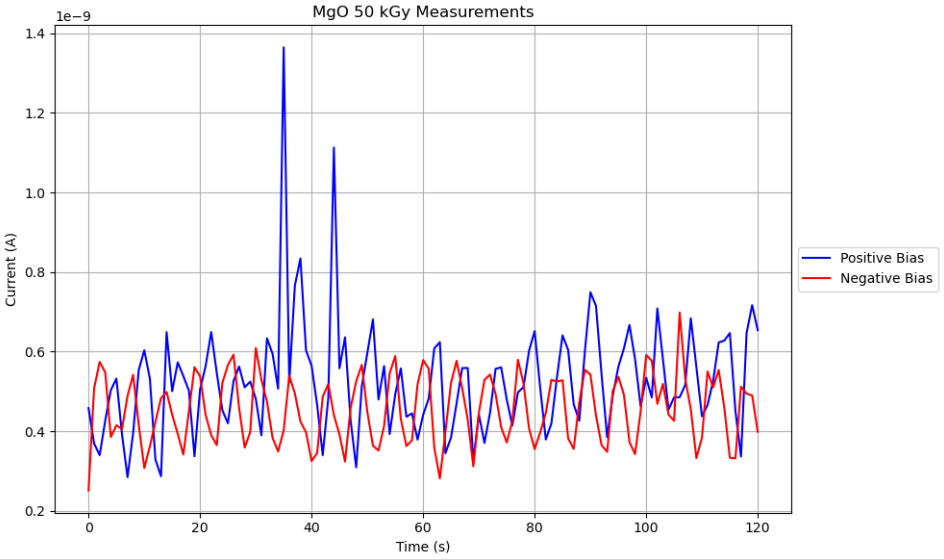


Figure 5.17: Measured current under positive and negative applied voltage bias for Magnesium Oxide samples with an absorbed gamma radiation dose of 50 kGy.

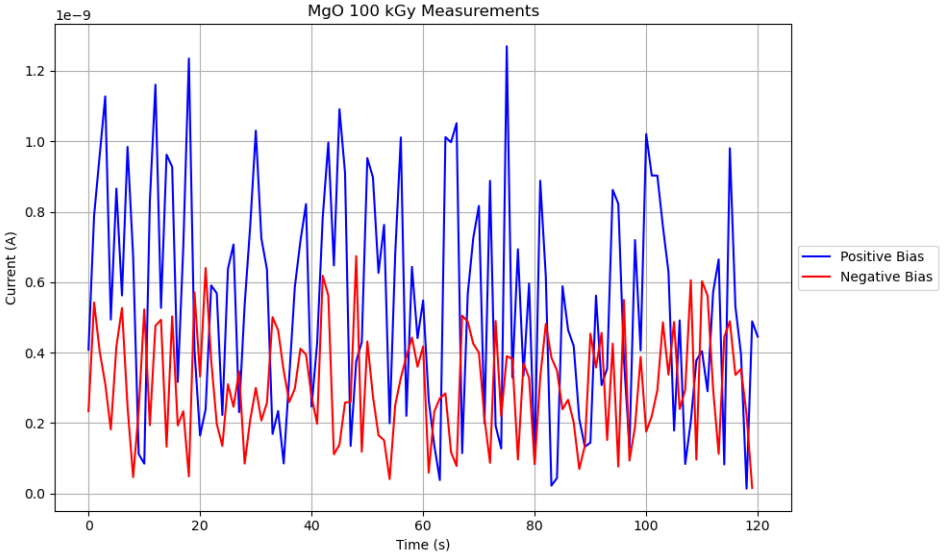


Figure 5.18: Measured current under positive and negative applied voltage bias for Magnesium Oxide samples with an absorbed gamma radiation dose of 100 kGy.

5.3.2 Aluminium Oxide

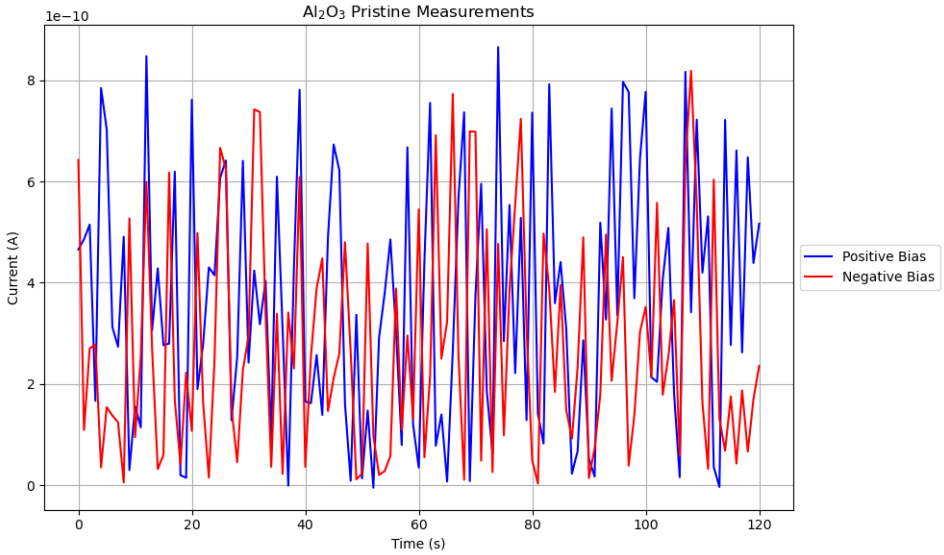


Figure 5.19: Measured current under positive and negative applied voltage bias for pristine Aluminium Oxide.

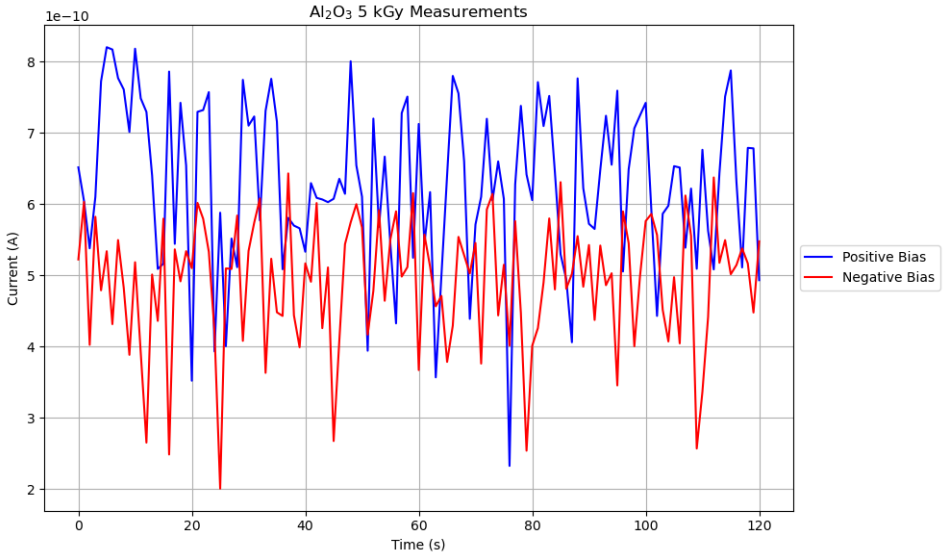


Figure 5.20: Measured current under positive and negative applied voltage bias for Aluminium Oxide samples with an absorbed gamma radiation dose of 5 kGy.

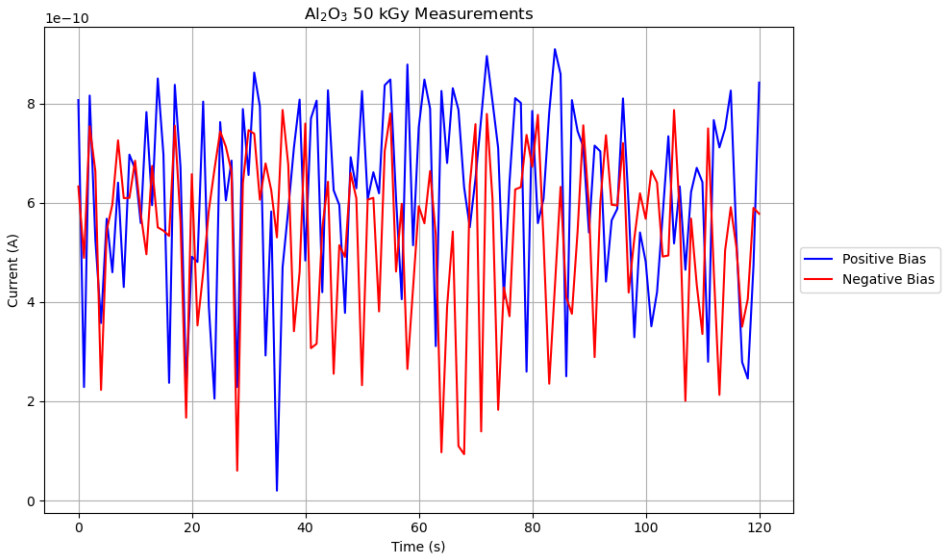


Figure 5.21: Measured current under positive and negative applied voltage bias for Aluminium Oxide samples with an absorbed gamma radiation dose of 50 kGy.

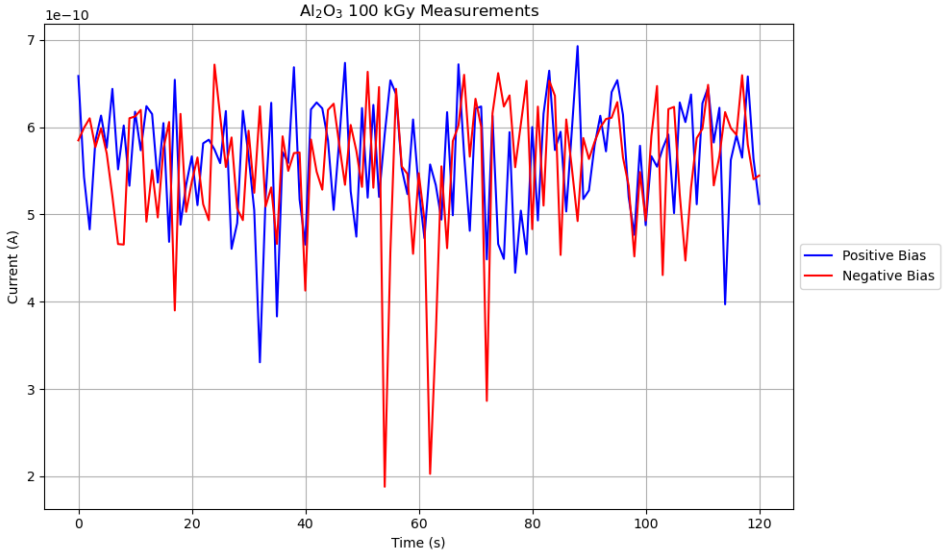


Figure 5.22: Measured current under positive and negative applied voltage bias for Aluminium Oxide samples with an absorbed gamma radiation dose of 100 kGy.

5.4 Averaged Current Measurements as a Function of Dose

The 120-second measurements at a rate of one measurement per second for each sample (5.3), for each specific bias and radiation dose, were averaged to produce a single value per sample. These average currents, plotted against the corresponding radiation dose, are presented below, with the error represented by the standard error (SE) of the mean.

$$SE = \pm \frac{\sigma}{\sqrt{N}} \tag{5.11}$$

Where σ is the standard deviation and N is the sample size.

$$SE = \pm \frac{\sqrt{\sum (x_i - \mu)^2}}{N\sqrt{N}} \tag{5.12}$$

Where x_i is the individual data points, μ is the mean of the data.

Table 5.1: Time-Averaged Current Measurements

Absorbed Dose	MgO Current (A)		Al_2O_3 Current (A)	
	Positive Bias	Negative Bias	Positive Bias	Negative Bias
Pristine (0 kGy)	$(3.86 \pm 0.052) \times 10^{-10}$	$(1.53 \pm 0.014) \times 10^{-10}$	$(3.64 \pm 0.226) \times 10^{-10}$	$(2.76 \pm 0.199) \times 10^{-10}$
5 kGy	$(6.06 \pm 0.176) \times 10^{-10}$	$(2.30 \pm 0.076) \times 10^{-10}$	$(6.27 \pm 0.104) \times 10^{-10}$	$(4.91 \pm 0.081) \times 10^{-10}$
50 kGy	$(5.27 \pm 0.130) \times 10^{-10}$	$(4.55 \pm 0.077) \times 10^{-10}$	$(6.14 \pm 0.175) \times 10^{-10}$	$(5.34 \pm 0.160) \times 10^{-10}$
100 kGy	$(5.46 \pm 0.290) \times 10^{-10}$	$(3.09 \pm 0.142) \times 10^{-10}$	$(5.63 \pm 0.061) \times 10^{-10}$	$(5.55 \pm 0.074) \times 10^{-10}$

The table above lists the time-averaged current measurements and their errors for positive bias (+500V) and negative bias (-500V) across various doses. These values are plotted on the next page and will be used to calculate the electronic emission yield of the samples.

5.4.1 Magnesium Oxide

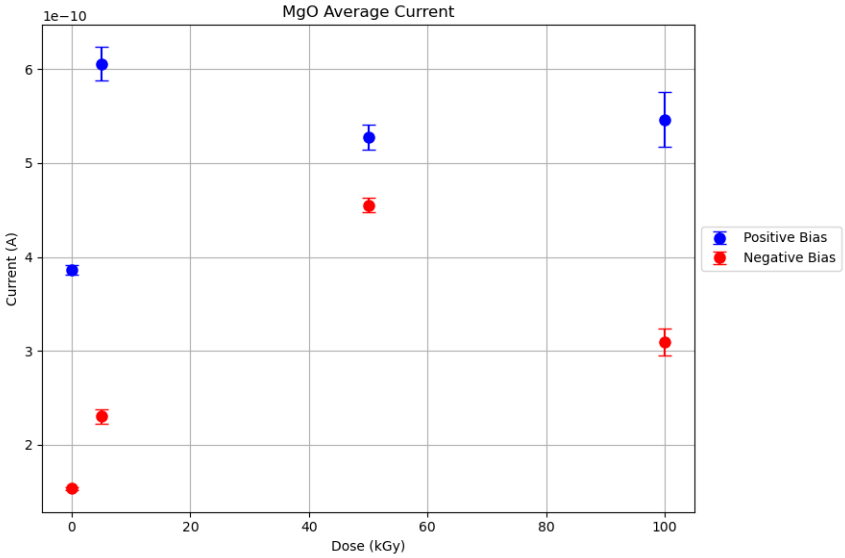


Figure 5.23: Averaged measured current under positive and negative applied bias for Magnesium Oxide samples as a function of absorbed gamma radiation dose.

5.4.2 Aluminium Oxide

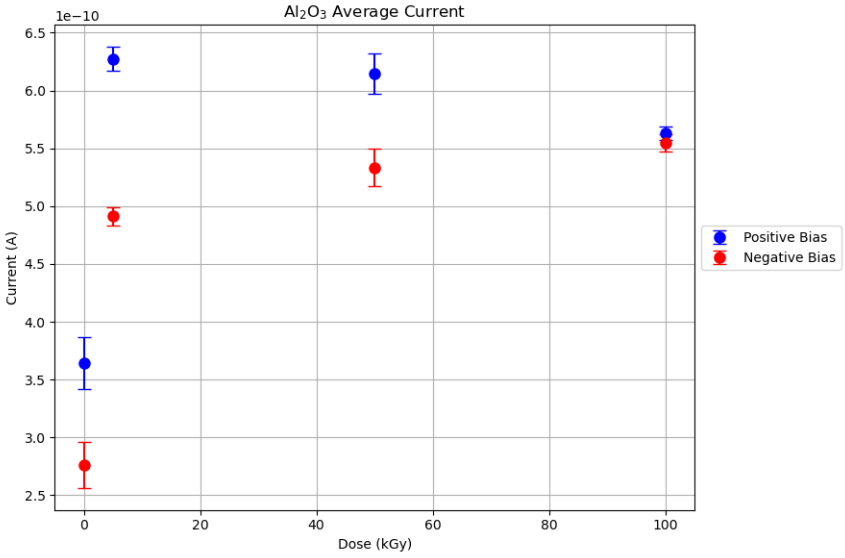


Figure 5.24: Averaged measured current under positive and negative applied bias for Aluminium Oxide samples as a function of absorbed gamma radiation dose.

5.4.3 Electron Emission Yield Measurements

The average current measurements (6.3) for each sample and each bias were then used in the electronic emission yield formula shown below:

$$\delta = \frac{\bar{I}^{+} - \bar{I}^{-}}{\bar{I}^{-}} \tag{5.13}$$

The related uncertainties for this calculation are given using uncertainty propagation:

Partial derivative with respect to $\bar{I}^{+}$:

$$\frac{\partial \delta}{\partial \bar{I}^{+}} = \frac{1}{\bar{I}^{-}} \tag{5.14}$$

Partial derivative with respect to $\bar{I}^{-}$:

$$\frac{\partial \delta}{\partial \bar{I}^{-}} = -\frac{\bar{I}^{+}}{(\bar{I}^{-})^{2}} \tag{5.15}$$

The uncertainty in the yield, σ_{δ}, is then calculated as:

$$\sigma_{\delta}^{2} = \left(\frac{\partial \delta}{\partial \bar{I}^{+}}\sigma_{\bar{I}^{+}}\right)^{2} + \left(\frac{\partial \delta}{\partial \bar{I}^{-}}\sigma_{\bar{I}^{-}}\right)^{2} \tag{5.16}$$

Substituting the derivatives:

$$\sigma_{\delta}^{2} = \left(\frac{\sigma_{\bar{I}^{+}}}{\bar{I}^{-}}\right)^{2} + \left(\frac{\bar{I}^{+}}{(\bar{I}^{-})^{2}}\sigma_{\bar{I}^{-}}\right)^{2} \tag{5.17}$$

Taking the square root:

$$\sigma_{\delta} = \sqrt{\left(\frac{\sigma_{\bar{I}^{+}}}{\bar{I}^{-}}\right)^{2} + \left(\frac{\bar{I}^{+}}{(\bar{I}^{-})^{2}}\sigma_{\bar{I}^{-}}\right)^{2}} \tag{5.18}$$

Where σ_{δ} represents the uncertainty in the electron emission yield, $\sigma_{\bar{I}^{+}}$ represents the uncertainty in $\bar{I}^{+}$, and $\sigma_{\bar{I}^{-}}$ represents the error in $\bar{I}^{-}$.

Where σ_{δ} represents the uncertainty in the electron emission yield, $\sigma_{\bar{I}^{+}}$ represents the uncertainty in $\bar{I^{+}}$, and $\sigma_{\bar{I}^{-}}$ represents the error in $\bar{I^{-}}$.

Table 5.2: Electron Yield Measurements

Absorbed Dose	MgO electronic emission yield	Al_2O_3 electronic emission yield
Pristine	1.5165 ± 0.2045	0.3191 ± 0.6175
5 kGy	1.6312 ± 0.5721	0.2772 ± 0.1471
50 kGy	0.1586 ± 0.170	0.1515 ± 0.2342
100 kGy	0.7671 ± 0.6110	0.0147 ± 0.0865

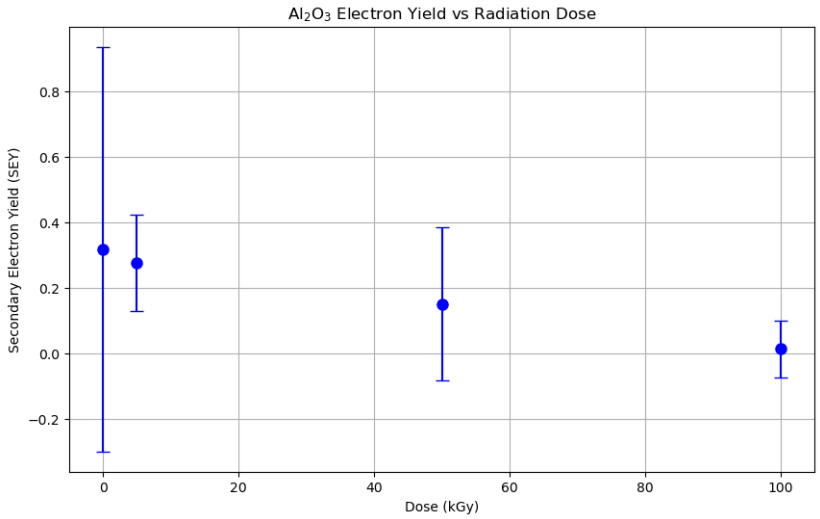


Figure 5.25: This figure presents the variation in electron emission yield of Aluminium Oxide as a function of radiation dose, illustrating how the material's electron emission yield responds to increasing gamma radiation exposure.

As shown in Table 5.2 and Figure 5.25, Aluminium Oxide demonstrates a proportional decrease between the absorbed gamma radiation dose and electron emission yield across all measured doses (0 kGy, 5 kGy, 50 kGy, and 100 kGy). The initial electron emission yield for the pristine sample is approximately 0.3191, but it steadily declines with increasing radiation dose, dropping to just 0.0147 at 100 kGy. This near-linear decrease highlights a proportional reduction in electron emission efficiency as a direct consequence of increased gamma radiation absorption in the 5 kGy samples. In contrast, for the 50 kGy and 100 kGy samples, the reduction can be attributed to the combined effects of increased gamma and beta radiation, which induce changes in the electronic properties of the material.

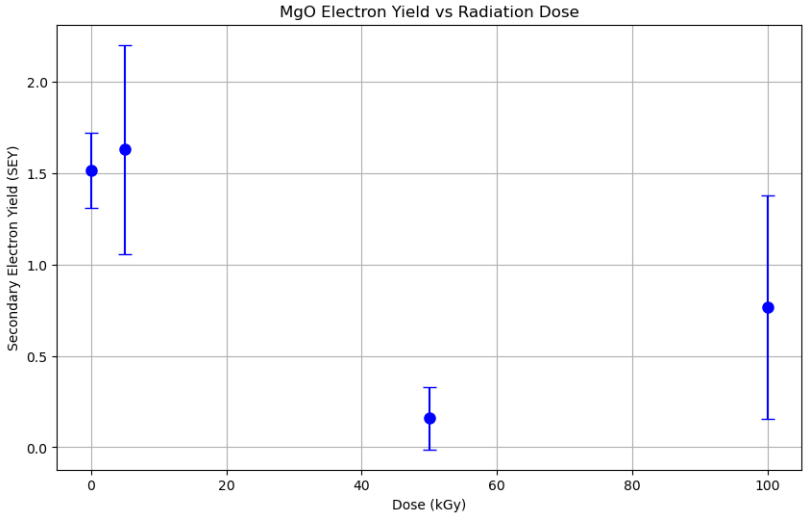


Figure 5.26: This figure presents the variation in electron emission yield of Magnesium Oxide as a function of radiation dose, illustrating how the material's electron emission yield responds to increasing gamma radiation exposure.

The pristine Magnesium Oxide sample exhibits an electron emission yield of 1.5165, while the sample irradiated to 100 kGy shows a yield of 0.7671. However, the 5 kGy sample displays an anomalously low electron emission yield of just 0.1586, deviating significantly from the behavior observed in the Aluminium Oxide samples. Despite this irregularity, Magnesium Oxide maintains a higher electron emission yield overall compared to Aluminium Oxide, even when accounting for the anomalous 5 kGy measurement.

This anomaly is likely due to localized surface contamination, given the powdered nature of the Magnesium Oxide samples and the 500 $\times$ 500 μm^2 scanning beam size, it is plausible that the specific region scanned during the 5 kGy measurement was compromised, leading to the unusually low yield.

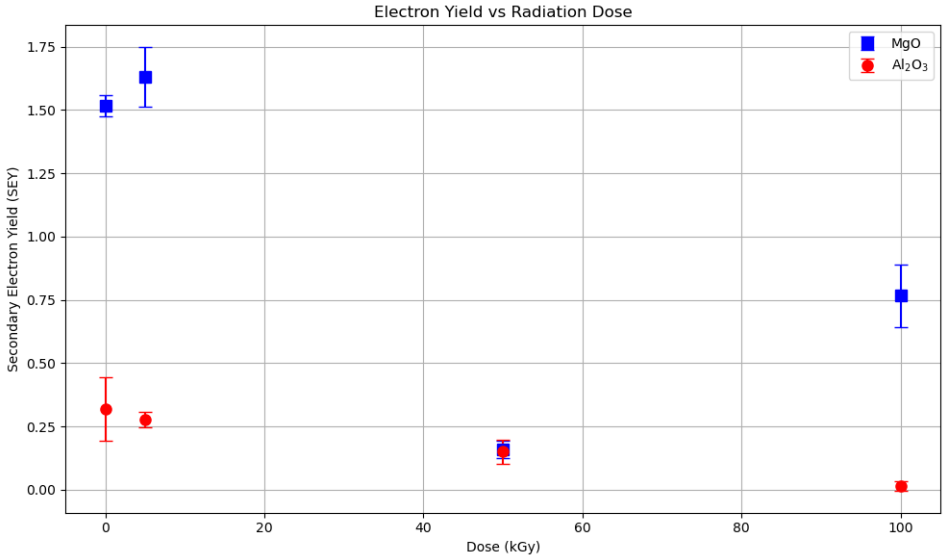


Figure 5.27: This figure presents the combined variation in electron emission yield of both Magnesium Oxide and Aluminium Oxide as a function of radiation dose, illustrating how the material's electron emission yield responds to increasing gamma radiation exposure.

As can be seen in Figure 5.27, aluminium oxide produces far fewer secondary electrons when compared to magnesium oxide. This stark difference in the SEY can be attributed to the significantly different activation energies for defect and charge migration in the two materials. For aluminium oxide, the activation energy associated with charge transport and oxygen self-diffusion ranges from approximately 440 to 730 kJ/mol [50], depending on factors such as crystallinity, grain boundary density, and temperature regime. In contrast, magnesium oxide exhibits a much lower activation energy of approximately 55 kJ/mol [51] for oxygen ion diffusion in the extrinsic regime. This implies that under irradiation, MgO allows electrons to migrate and escape the surface more easily than Al_2O_3, leading to a substantially higher secondary electron yield. The higher activation energy of Al_2O_3 suggests that electron mobility is more restricted, thereby suppressing secondary electron emission.

Aluminium Oxide in contrast follows a systematic and reproducible trend, reinforcing the reliability of its dose-dependent response. The inverse relationship observed aligns with previous studies, as illustrated by the following literature extracts:

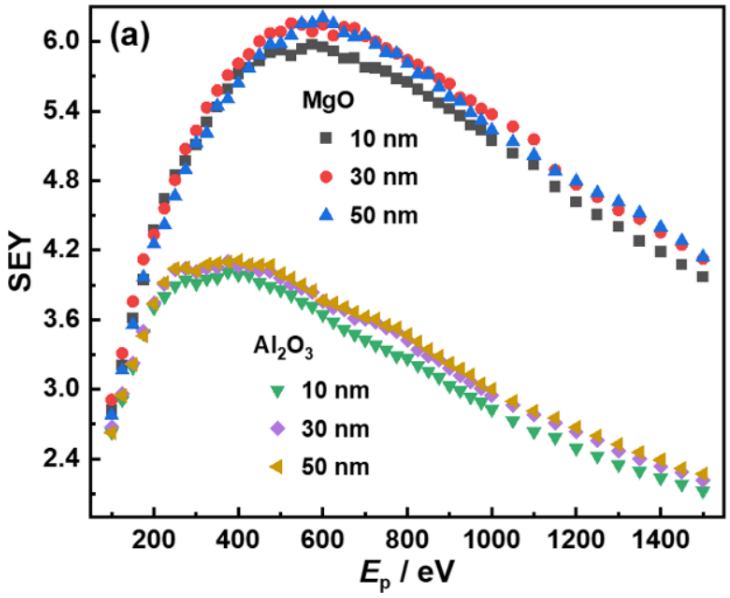


Figure 5.28: Secondary electron yield as a function of the primary electron energy for Aluminium Oxide and Magnesium Oxide thin films at varying film thickness [52].

Figure 5.28 provides context by comparing the measured electron emission yield values from this study with those reported in the literature. As shown in the figure, the electron emission yield values for Magnesium Oxide are generally higher than those for Aluminium Oxide, which is consistent with the findings of this study.

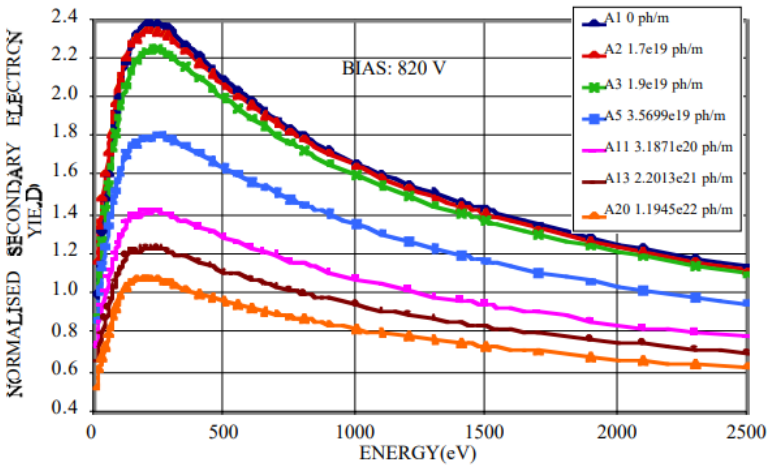


Figure 5.29: Normalized electron emission yield for a Copper sample at varying levels of absorbed radiation dose induced by photons [53].

Figure 5.29 shows the variation in electron emission yield as a function of electron dose

for a copper sample subjected to el78 / 87 Development of new radiation hard materials with high secondary electron emission yield for the nuclear industry Cameron Lance Baldwin A report submitted as the requirements for an MSc by dissertation The University of the Witwatersrand School of Physics Johannesburg, South Africa July 2025 Supervisor Professor Elias Sideras-Haddad Figure 5.27: This figure presents the combined variation in electron emission yield of both Magnesium Oxide and Aluminium Oxide as a function of radiation dose, illustrating how the material's electron emission yield responds to increasing gamma radiation exposure. As can be seen in Figure 5.27, aluminium oxide produces far fewer secondary elec- trons when compared to magnesium oxide. This stark difference in the SEY can be attributed to the significantly different activation energies for defect and charge migra- tion in the two materials. For aluminium oxide, the activation energy associated with charge transport and oxygen self-diffusion ranges from approximately 440 to 730 kJ/mol [50], depending on factors such as crystallinity, grain boundary density, and temper- ature regime. In contrast, magnesium oxide exhibits a much lower activation energy of approximately 55 kJ/mol [51] for oxygen ion diffusion in the extrinsic regime. This implies that under irradiation, MgO allows electrons to migrate and escape the surface more easily than Al2O3, leading to a substantially higher secondary electron yield. The higher activation energy of Al2O3 suggests that electron mobility is more restricted, thereby suppressing secondary electron emission. Aluminium Oxide in contrast follows a systematic and reproducible trend, reinforcing the reliability of its dose-dependent response. The inverse relationship observed aligns with previous studies, as illustrated by the following literature extracts: 63 Figure 5.28: Secondary electron yield as a function of the primary electron energy for Aluminium Oxide and Magnesium Oxide thin films at varying film thickness [52]. Figure 5.28 provides context by comparing the measured electron emission yield values from this study with those reported in the literature. As shown in the figure, the electron emission yield values for Magnesium Oxide are generally higher than those for Aluminium Oxide, which is consistent with the findings of this study. Figure 5.29: Normalized electron emission yield for a Copper sample at varying levels of ab- sorbed radiation dose induced by photons [53]. Figure 5.29 shows the variation in electron emission yield as a function of electron 64 ectron scrubbing [53]. This figure illustrates a dose-dependent decline in SEY, where radiation-induced surface modifications, such as defect formation and surface roughening, lead to a reduction in the material's electron emission efficiency. A similar trend is observed in this study for Aluminium Oxide, where increasing gamma radiation dose results in a proportional decline in SEY, indicating that similar damage mechanisms may be at play despite the difference in material class, as copper is a metal and Aluminium Oxide is an insulator.

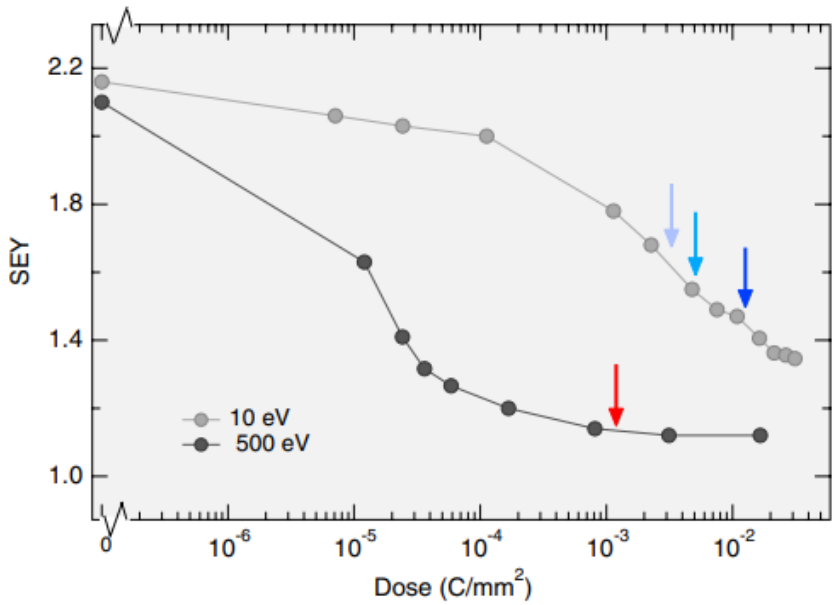


Figure 5.30: SEY as a function of the absorbed electron dose on a copper sample, based on [54], for an electron energy of 500 eV (dark gray) and 10 eV (gray).

Figure 5.30 shows the variation in electron emission yield as a function of electron dose for a copper sample subjected to electron scrubbing [54]. This figure illustrates the proportional decrease between electron dose and SEY, where radiation-induced surface modifications, such as defect formation and surface roughening, lead to a reduction in the material's electron emission efficiency. A similar trend is observed in this study for Aluminium Oxide, where increasing gamma radiation dose results in a proportional decline in SEY, indicating that similar damage mechanisms may be at play despite the difference in material class, as copper is a metal and Aluminium Oxide is an insulator.

As discussed in Section 2.3, the inverse relationship between radiation dose and electron emission yield can be explained by the interaction mechanisms of high-energy photons emitted from Co-60 sources. These gamma rays induce ionization within the samples through the photoelectric effect, Compton scattering, and pair production. The resulting ionization generates electron-hole pairs, with displaced electrons possessing sufficient energy to further dislodge atoms, creating vacancies as well as interstitials which in turn means that structural defects are present within the samples [55].

Chapter 6

Conclusion

6.1 Conclusions

Dynodes form the basis for the working mechanism of photomultiplier tubes, dynodes are constantly subject to extreme radiation environments and as a result show a diminishing gain due to a loss of secondary electron yield as a function of time. It is therefore imperative to explore new materials which could prove to be suitable dynode materials.

In this study, Al_2O_3 and MgO samples were investigated as potential dynode materials and were subjected to high levels of gamma radiation at the CERN Co-60 facility. The chosen radiation doses were selected to match the exposure levels experienced by PMTs in the CERN ATLAS detector.

Simulations of these irradiation were performed to simulate the displacements per atom as well as the absorbed dose each sample suffered due to the radiation damage. The simulations clearly showed that the target doses were reached and that as the radiation dose increased so too did the displacements per atom.

The EEY of the samples was measured at the TAMS facility at iThemba LABS, revealing a clear trend as a function of radiation dose. This trend was particularly evident in the Al_2O_3 samples, which exhibited an approximately linear decrease in EEY with increasing dose. The MgO samples followed a similar overall pattern, though with notable deviations. The 5 kGy MgO sample displayed a higher EEY than the pristine sample, while the 50 kGy MgO sample exhibited an unexpectedly low EEY. This anomaly is likely due to compromised sample integrity.

The EEY reduction as a percentage of the pristine EEY is shown below for doses of 5kGy, 50kGy, and 100kGy:

	5kGy	50kGy	100kGy
Al_2O_3	$86.87 \pm 29.94\%$	$47.48 \pm 23.03\%$	$4.61 \pm 4.71\%$
MgO	$107.56 \pm 8.80\%$	$10.46 \pm 2.14\%$	$50.58 \pm 7.84\%$

Table 6.1: EEY as a function of their pristine samples EEY

As shown in Table 6.1 and discussed in the Results section, the EEY of MgO, excluding the 50 kGy sample, is generally higher than that of Al_2O_3. Additionally, the decrease in EEY with increasing dose is less pronounced for MgO, indicating a more gradual drop-off compared to Al_2O_3.

6.2 Future Work

This study demonstrates significant potential in determining the EEY of materials as a function of radiation dose. Future work will focus on expanding the scope of materials tested to assess their viability as dynode candidates. Future work will include an electron source to determine the SEY of the materials as opposed to their EEY.

Furthermore, investigations using different radiation sources, such as heavy ions or pulsed electron beams, will provide insight into how EEY behavior varies under different irradiation conditions. Advanced surface characterization techniques, such as X-ray photoelectron spectroscopy (XPS) and scanning electron microscopy (SEM), will also be incorporated to correlate EEY changes with surface modifications at the microscopic level. These efforts will contribute to a more detailed understanding of radiation-induced effects, ultimately guiding the development of more resilient and efficient dynode materials.

Bibliography

[1] ATLAS Collaboration. "ATLAS Event Display of first 13.6 TeV Collisions starting Run 3". General Photo. 2024. URL: https://cds.cern.ch/record/2894733.

[2] Benjamin Nachman. *Modeling Radiation Damage to Pixel Sensors in the ATLAS Detector*. 2017. arXiv: 1710.03916 [physics.ins-det]. URL: https://arxiv.org/abs/1710.03916.

[3] Kacper Bilko et al. "Radiation Environment in the Large Hadron Collider During the 2022 Restart and Related RHA Implications". In: *IEEE Transactions on Nuclear Science* PP (Jan. 2023), pp. 1–1. DOI: 10.1109/TNS.2023.3328145.

[4] Hamamatsu Photonics. *Photomultiplier Tubes: Basics and Applications*. Accessed: 2025-01-07, see p. 39. 2017. URL: https://www.hamamatsu.com/content/dam/hamamatsu-photonics/sites/documents/99_SALES_LIBRARY/etd/PMT_handbook_v4E.pdf.

[5] Rachel Yotter and Denise Wilson. "A review of photodetectors for sensing light-emitting reporters in biological systems". In: *Sensors Journal, IEEE* 3 (July 2003), pp. 288–303. DOI: 10.1109/JSEN.2003.814651.

[6] Nathan Haboury and Edward Galantay. "Lifetime of muon". In: (July 2020).

[7] Chuanya Cao et al. "Mass production and characterization of 3-inch PMTs for the JUNO experiment". In: *Nuclear Instruments and Methods in Physics Research Section A: Accelerators, Spectrometers, Detectors and Associated Equipment* 1005 (2021), p. 165347. ISSN: 0168-9002. DOI: https://doi.org/10.1016/j.nima.2021.165347. URL: https://www.sciencedirect.com/science/article/pii/S0168900221003314.

[8] Georges Aad et al. "The ATLAS experiment at the CERN Large Hadron Collider: a description of the detector configuration for Run 3". In: *JINST* 19.05 (2024), P05063. DOI: 10.1088/1748-0221/19/05/P05063. arXiv: 2305.16623 [physics.ins-det].

[9] D. Boumediene. "Calibration and monitoring systems of the ATLAS tile hadron calorimeter". In: *Nuclear Instruments and Methods in Physics Research Section A: Accelerators, Spectrometers, Detectors and Associated Equipment* 718 (2013).

Proceedings of the 12th Pisa Meeting on Advanced Detectors, pp. 66–68. ISSN: 0168-9002. DOI: https://doi.org/10.1016/j.nima.2012.11.070. URL: https://www.sciencedirect.com/science/article/pii/S0168900212014076.

[10] Anton Lechner. "Particle interactions with matter". In: *CERN Yellow Rep. School Proc.* 5 (2018), p. 47. DOI: 10.23730/CYRSP-2018-005.47. URL: https://cds.cern.ch/record/2674116.

[11] Hadar Lazar. "The Atlas Tile Calorimeter experience with 10,000 readout photomultipliers operating since the start of the p-p collisions at LHC". In: *Nuclear Instruments and Methods in Physics Research Section A: Accelerators, Spectrometers, Detectors and Associated Equipment* 912 (2018). New Developments In Photodetection 2017, pp. 248–251. ISSN: 0168-9002. DOI: https://doi.org/10.1016/j.nima.2017.11.068. URL: https://www.sciencedirect.com/science/article/pii/S0168900217313141.

[12] M.N. Agaras et al. "Laser calibration of the ATLAS Tile Calorimeter during LHC Run 2". In: *Journal of Instrumentation* 18.06 (June 2023), P06023. ISSN: 1748-0221. DOI: 10.1088/1748-0221/18/06/p06023. URL: http://dx.doi.org/10.1088/1748-0221/18/06/P06023.

[13] Nuno Filipe Viseu Duarte. "Proportional Counters Equipped with Thin B4C Conversion Layers for the Detection of Slow Neutrons". PhD thesis. University of Coimbra, 2022. URL: https://hdl.handle.net/10316/100420.

[14] U.S. Nuclear Regulatory Commission. *Interaction of Charged Particles with Matter*. NUREG/CR-XXXX, Module 2 of Basic Health Physics. Mar. 2011. URL: https://www.nrc.gov/docs/ml1122/ml11229a666.pdf.

[15] William R. Leo. *Techniques for Nuclear and Particle Physics Experiments: A How-To Approach*. 2nd. Berlin, Heidelberg: Springer, 1994.

[16] Syed Naeem Ahmed. "2 - Interaction of radiation with matter". In: *Physics and Engineering of Radiation Detection (Second Edition)*. Ed. by Syed Naeem Ahmed. Second Edition. Elsevier, 2015, pp. 65–155. ISBN: 978-0-12-801363-2. DOI: https://doi.org/10.1016/B978-0-12-801363-2.00002-4. URL: https://www.sciencedirect.com/science/article/pii/B9780128013632000024.

[17] Chen-Kai Qiao, Jian-Wei Wei, and Lin Chen. "An Overview of the Compton Scattering Calculation". In: *Crystals* 11.5 (2021). ISSN: 2073-4352. DOI: 10.3390/cryst11050525. URL: https://www.mdpi.com/2073-4352/11/5/525.

[18] Pete Karpius and Terence Reilly. "Gamma-Ray Interactions with Matter". In: Oct. 2024, pp. 27–41. ISBN: 978-3-031-58276-9. DOI: 10.1007/978-3-031-58277-6_3.

[19] MICHAEL F. L'ANNUNZIATA. "1 - NUCLEAR RADIATION, ITS INTERACTION WITH MATTER AND RADIOISOTOPE DECAY". In: *Handbook of*

Radioactivity Analysis (Second Edition). Ed. by Michael F. L'Annunziata. Second Edition. San Diego: Academic Press, 2003, pp. 1–121. DOI: https://doi.org/10.1016/B978-012436603-9/50006-5. URL: https://www.sciencedirect.com/science/article/pii/B9780124366039500065.

[20] Shu Tao, Hong Chan, and Harry Graaf. "Secondary Electron Emission Materials for Transmission Dynodes in Novel Photomultipliers: A Review". In: *Materials* 9 (Dec. 2016). DOI: 10.3390/ma9121017.

[21] J. E. Yater. "Secondary electron emission and vacuum electronics". In: *Journal of Applied Physics* 133.5 (Feb. 2023), p. 050901. ISSN: 0021-8979. DOI: 10.1063/5.0130972. eprint: https://pubs.aip.org/aip/jap/article-pdf/doi/10.1063/5.0130972/20007922/050901_1_5.0130972.pdf. URL: https://doi.org/10.1063/5.0130972.

[22] A. Shih et al. "Secondary electron emission studies". In: *Applied Surface Science* 111 (1997). Proceedings of the International Vacuum Electron Sources Conference 1996, pp. 251–258. ISSN: 0169-4332. DOI: https://doi.org/10.1016/S0169-4332(96)00729-5. URL: https://www.sciencedirect.com/science/article/pii/S0169433296007295.

[23] A. Hussain et al. "Theoretical calculations of the mean escape depth of secondary electron emission from compound semiconductor materials". In: *Journal of Applied Physics* 127.12 (Mar. 2020), p. 125304. ISSN: 0021-8979. DOI: 10.1063/1.5144721. eprint: https://pubs.aip.org/aip/jap/article-pdf/doi/10.1063/1.5144721/15244163/125304_1_online.pdf. URL: https://doi.org/10.1063/1.5144721.

[24] Tomas Martin. "Lithium oxygen termination as a negative electron affinity surface on diamond: a computational and photoemission study". PhD thesis. July 2011. DOI: 10.13140/RG.2.1.4380.0561.

[25] Xiangping Zhu et al. "Evolvement Investigation of Secondary Electron Emission for Ultrathin MgO Coatings Prepared by Atomic Layer Deposition". In: *Applied Sciences* 11.11 (2021). ISSN: 2076-3417. DOI: 10.3390/app11114801. URL: https://www.mdpi.com/2076-3417/11/11/4801.

[26] A. A. Manalio, K. Burin, and G. M. Rothberg. "More efficient channel electron multiplier by coating of the cone with a high secondary electron yield material". In: *Review of Scientific Instruments* 52.10 (Oct. 1981), pp. 1490–1492. ISSN: 0034-6748. DOI: 10.1063/1.1136481. eprint: https://pubs.aip.org/aip/rsi/article-pdf/52/10/1490/19054027/1490_1_online.pdf. URL: https://doi.org/10.1063/1.1136481.

[27] Qi He et al. "High-dose X-ray radiation induced MgO degradation and breakdown in spin transfer torque magnetic tunnel junctions". In: *Scientific Reports* 12.1

(2022), p. 18620. ISSN: 2045-2322. DOI: 10.1038/s41598-022-19342-x. URL: https://doi.org/10.1038/s41598-022-19342-x.

[28] Junjiang Guo et al. "Secondary electron emission characteristics of Al2O3 coatings prepared by atomic layer deposition". In: *AIP Advances* 9.9 (Sept. 2019), p. 095303. ISSN: 2158-3226. DOI: 10.1063/1.5113671. eprint: https://pubs.aip.org/aip/adv/article-pdf/doi/10.1063/1.5113671/13107008/095303_1_online.pdf. URL: https://doi.org/10.1063/1.5113671.

[29] N.R. Rajopadhye, S.B. Dake, and S.V. Bhoraskar. "Characterization of Al2O3 films deposited by various methods". In: *Thin Solid Films* 142.1 (1986), pp. 127–138. ISSN: 0040-6090. DOI: https://doi.org/10.1016/0040-6090(86)90308-1. URL: https://www.sciencedirect.com/science/article/pii/0040609086903081.

[30] Chang-Sheng Zha, Ho-kwang Mao, and Russell J. Hemley. "Elasticity of MgO and a primary pressure scale to 55 GPa". In: *Proceedings of the National Academy of Sciences* 97.25 (2000), pp. 13494–13499. DOI: 10.1073/pnas.240466697. eprint: https://www.pnas.org/doi/pdf/10.1073/pnas.240466697. URL: https://www.pnas.org/doi/abs/10.1073/pnas.240466697.

[31] A S Sharipov, B I Loukhovitski, and A M Starik. "Theoretical study of structure and physical properties of (Al2O3)n clusters". In: *Physica Scripta* 88.5 (Oct. 2013), p. 058307. DOI: 10.1088/0031-8949/88/05/058307. URL: https://dx.doi.org/10.1088/0031-8949/88/05/058307.

[32] CERN. *ATLAS Experiment*. Accessed: 2025-03-04. 2025. URL: https://home.cern/science/experiments/atlas.

[33] University of Chicago ATLAS Group. *ATLAS Tile Calorimeter (TileCal)*. Accessed: 2025-03-04. 2025. URL: https://hep.uchicago.edu/atlas/tilecal/.

[34] ATLAS Collaboration. *Rapidity - ATLAS Glossary*. Accessed: 2025-03-04. 2025. URL: https://atlas.cern/glossary/rapidity.

[35] M Aaboud et al. "Operation and performance of the ATLAS Tile Calorimeter in Run 1". In: *The European Physical Journal C* 78.12 (Nov. 2018), p. 987. ISSN: 1434-6044. DOI: 10.1140/epjc/s10052-018-6374-z. URL: https://doi.org/10.1140/epjc/s10052-018-6374-z.

[36] Jacob Van Dyk, Jerry J Battista, and PR Almond. "A retrospective of cobalt-60 radiation therapy: the atom bomb that saves lives". In: *Medical Physics International Journal, Special Issue, History of Medical Physics* 4 (2020).

[37] Sajid Ahmad, Raheel Hammad, and Seemin Rubab. "Gamma Radiation-Induced Synthesis of Polyaniline-Based Nanoparticles/Nanocomposites". In: *Journal of Electronic Materials* 51 (July 2022). DOI: 10.1007/s11664-022-09823-0.

[38] E C Amato et al. “Measurement of the angular correlation between the two gamma rays emitted in the radioactive decays of a 60Co source with two NaI(Tl) scintillators”. In: *European Journal of Physics* 43.5 (July 2022), p. 055802. ISSN: 1361-6404. DOI: 10.1088/1361-6404/ac78a3. URL: http://dx.doi.org/10.1088/1361-6404/ac78a3.

[39] Patricia Paladino et al. “PLATAGAM: a videogame structured as a didactical material for divulgation of some of the benefits of the Gamma Radiation produced in the Cobalt-60 Multipurpose Irradiator at IPEN’s facilities”. In: *Brazilian Journal of Radiation Sciences* 10 (Oct. 2022). DOI: 10.15392/2319-0612.2022.1851.

[40] Faïçal Azaiez et al. “iThemba LABS”. In: *Nuclear Physics News* 30.4 (2020), pp. 5–11. DOI: 10.1080/10619127.2020.1832807. eprint: https://doi.org/10.1080/10619127.2020.1832807. URL: https://doi.org/10.1080/10619127.2020.1832807.

[41] Mlungisi Nkosi. *Ion Beam Analysis at iThemba LABS TAMS*. Presentation at the African Conference on Physics (ACP 2023). 2023. URL: https://indico.cern.ch/event/1229551/contributions/5525333/attachments/2724404/4734271/ACP2023_Mlungisi_Nkosi_29Sept2023.pdf.

[42] D.B. Rebuli, E. Sideras-Haddad, and S.H. Connell. “Emission of electrons from diamond surfaces induced by MeV ions”. In: *Nuclear Instruments and Methods in Physics Research Section B: Beam Interactions with Materials and Atoms* 219-220 (2004). Proceedings of the Sixteenth International Conference on Ion Beam Analysis, pp. 299–302. ISSN: 0168-583X. DOI: https://doi.org/10.1016/j.nimb.2004.01.072. URL: https://www.sciencedirect.com/science/article/pii/S0168583X04001004.

[43] C. Ahdida et al. “New Capabilities of the FLUKA Multi-Purpose Code”. In: *Frontiers in Physics* 9 (2022), p. 788253. URL: https://fluka.cern.

[44] G. Battistoni et al. “Overview of the FLUKA code”. In: *Annals of Nuclear Energy* 82 (2015), pp. 10–18. URL: https://fluka.cern.

[45] Alberto Fasso et al. “FLUKA Realistic Modeling of Radiation Induced Damage”. In: *Progress in NUCLEAR SCIENCE and TECHNOLOGY* 2 (Oct. 2011), pp. 769–775. DOI: 10.15669/pnst.2.769.

[46] V. Vlachoudis. “FLAIR: A Powerful But User Friendly Graphical Interface For FLUKA”. In: *Proc. Int. Conf. on Mathematics, Computational Methods & Reactor Physics (M&C 2009)*. Saratoga Springs, New York, 2009.

[47] Alberto Fasso et al. “FLUKA Realistic Modeling of Radiation Induced Damage”. In: *Progress in NUCLEAR SCIENCE and TECHNOLOGY* 2 (Oct. 2011), pp. 769–775. DOI: 10.15669/pnst.2.769.

[48] National Institute of Standards and Technology (NIST). *ESTAR: Stopping-Power and Range Tables for Electrons, Protons, and Helium Ions*. Accessed: 2025-02-05. 2025. URL: https://physics.nist.gov/PhysRefData/Star/Text/ESTAR.html.

[49] T.A. Nguyen, C. Rangacharyulu, and C.V. Tao. "Depth-Dose Distribution Dependence on the Energy Profile of Linear and Laser Wakefield Accelerator Electron Beams". In: *Proc. IPAC'21* (Campinas, SP, Brazil). International Particle Accelerator Conference 12. https://doi.org/10.18429/JACoW-IPAC2021-TUPAB416. JACoW Publishing, Geneva, Switzerland, Aug. 2021, TUPAB416, pp. 2502–2505. ISBN: 978-3-95450-214-1. DOI: 10.18429/JACoW-IPAC2021-TUPAB416. URL: https://jacow.org/ipac2021/papers/tupab416.pdf.

[50] Jenqdaw Wang and Rishi Raj. "Estimate of the Activation Energies for Boundary Diffusion from Rate-Controlled Sintering of Pure Alumina, and Alumina Doped with Zirconia or Titania". In: *Journal of the American Ceramic Society* 73.5 (1990), pp. 1172–1175. DOI: https://doi.org/10.1111/j.1151-2916.1990.tb05175.x. eprint: https://ceramics.onlinelibrary.wiley.com/doi/pdf/10.1111/j.1151-2916.1990.tb05175.x. URL: https://ceramics.onlinelibrary.wiley.com/doi/abs/10.1111/j.1151-2916.1990.tb05175.x.

[51] Rohan Singh Pal et al. "Highly active and selective Li/MgO catalysts for methane transformation to C2 hydrocarbons: experimental and DFT study". In: *Energy Adv.* 2.1 (2023), pp. 180–197. DOI: 10.1039/D2YA00096B. URL: http://dx.doi.org/10.1039/D2YA00096B.

[52] Zhuoxi Lian et al. "Effect of atmospheric environment on the stability of secondary electron emission from magnesium oxide and alumina surfaces". In: *Journal of Physics D: Applied Physics* 57 (Dec. 2023). DOI: 10.1088/1361-6463/ad15c0.

[53] Vincent Baglin et al. "The Secondary Electron Yield of Technical Materials and its Variation with Surface Treatments". In: June 2000.

[54] R. Larciprete et al. "Secondary electron yield of Cu technical surfaces: Dependence on electron irradiation". In: *Phys. Rev. ST Accel. Beams* 16 (1 Jan. 2013), p. 011002. DOI: 10.1103/PhysRevSTAB.16.011002. URL: https://link.aps.org/doi/10.1103/PhysRevSTAB.16.011002.

[55] Ruchi Bisht and Anjum Begum. "Gamma-Irradiation Effects on Different Metal Oxide Nanoparticles". In: *Futuristic Trends in Chemical, Material Sciences & Nano Technology*. Vol. 3. IIP Series 9. International Innovative Publications, 2024. Chap. 4, pp. 126–140. URL: https://www.iipseries.org/assets/docupload/rsl2024E422C17F996BBB2.pdf.